Russian Chemical Reviews **80** (6) 579 – 604 (2011) © 2011 Russian Academy of Sciences and Turpion Ltd

DOI 10.1070/RC2011v080n06ABEH004187

Magnetometric methods of investigation of supported catalysts

P A Chernavskii, G V Pankina, V V Lunin

Contents

I.	Introduction	579
II.	Non-resonance magnetic methods of investigation of catalysts	580
III.	Single-domain and superparamagnetic metal particles	581
IV.	Magnetic granulometry methods	583
V.	Magnetization of metal particles and adsorption of molecules from the gas phase on them	586
VI.	Supported catalysts as systems of nanoparticles	587
VII.	Topochemical processes on Fe-containing catalysts	588
VIII.	Topochemical processes on Co-containing catalysts	595
IX.	Nickel-containing catalysts	601
X.	Comparison of magnetometric methods with other methods of investigation of supported catalysts	601
XI.	Conclusion	602

Abstract. The most recent advances in magnetometric methods of investigation of supported Co-, Ni- and Fe-containing catalysts are outlined. Magnetic characteristics provide comprehensive information on (i) catalytic reactions, (ii) the size and distribution of ferromagnetic nanoparticles in topochemical reactions during the catalyst preparation and in the catalytic process and (iii) chemisorption on ferromagnets. The characteristic features and advantages of different magnetometric methods and their combinations with traditional methods of investigation of catalysts are considered. The bibliography includes 148 references.

I. Introduction

Supported catalysts based on iron subgroup metals (Co, Ni and Fe) are widely used in industrial catalysis. Recently, interest in such systems has increased, in particular, due to the growing demand for environmentally safe liquid fuels and the need for utilization of associated petroleum gases that are now burnt in flares.[1–3] Research on these catalysts has been well documented. Most studies concern the structure of Co- and Fe-containing catalysts because they are used in industrial catalysis.

P A Chernavskii, G V Pankina, V V Lunin Department of Chemistry, M V Lomonosov Moscow State University, Leninskie Gory 1, 119991 Moscow, Russian Federation. Fax (7-495) 932 88 46, tel. (7-495) 939 49 13, e-mail: chern@kge.msu.ru, chern5@inbox.ru (P A Chernavskii), pankina@kge.msu.ru, pankina5151@inbox.ru (G V Pankina), tel. (7-495) 939 45 75, (7-495) 939 3571, e-mail: vvlunin@kge.msu.ru (V V Lunin)

Received 17 September 2010
Uspekhi Khimii **80** (6) 605 – 632 (2011); translated by A M Raevskij

Usually, problems faced by researchers are due to relatively high reactivity of very small particles of iron subgroup metals and their oxides. This first of all concerns the interaction of metals and their oxides with supports (Al_2O_3, SiO_2, TiO_2 *etc.*).[4] When highly dispersed, these metals readily react with the reaction medium, which suggests the occurrence of topochemical processes in the supported catalysts. Among them, there are the oxidation of metals by trace amounts of oxygen and water; carburization, which often accompanies transformations of monocarbon molecules, the formation of nitrides, sulfides, *etc.* Clearly, in the development of efficient catalytic processes one should have comprehensive information on the accompanying topochemical reactions, which often change the activities and selectivities of catalysts. Modern methods of investigation of topochemical reactions in systems containing nanoparticles (particles of size less than < 100 nm) do not always provide reliable data on the kinetics and mechanisms of these processes. Magnetometric methods appeared to be highly efficient in solving many problems which pose in studies of supported catalysts based on ferromagnetic metals (Fe, Co, Ni).[5]

A specific problem consists in the determination of the degree of dispersion (or size) of metal particles in the metal-based catalysts. Obtaining information on the structure formation of a catalyst in the course of its preparation and immediately in the catalytic reaction faces severe difficulties (exceptions are the *in situ* and *operando* methods). A comparative analysis of modern methods of investigation of Co-containing supported catalysts for the Fischer – Tropsch synthesis was reported.[1]

High-resolution transmission electron microscopy (HR TEM) enables direct determination of the particle sizes and the particle size distribution. However, this method is not always applicable to the systems in question and gives reasonable results only for such supports as

carbonaceous materials or silica gel. Methods for the determination of the particle size of supported metals based on X-ray scattering may also fail to establish the size distribution of metal particles, especially in the case of multimodal distributions. Often, problems in understanding the mechanisms of topochemical reactions on supported catalysts containing Co, Ni and Fe as the active components can be solved only using magnetic granulometry methods.[6–9]

This review is devoted to the most recent advances in the magnetometric methods of investigation of metal-containing (especially, metal-supported) catalysts, which use the magnetization as the key parameter. The emphasis is placed on the Fischer–Tropsch synthesis and some other catalytic processes involving such ferromagnetic systems as catalysts.

II. Non-resonance magnetic methods of investigation of catalysts

Classical methods of investigation of magnetic properties can be divided into two groups, *viz*., static methods and dynamic ones. Catalysts can be studied by all of them. However, peculiar features of the systems in question impose specific requirements to the magnetometric equipment that should enable *in situ* measurements in a controllable gaseous medium and in a temperature range as wide as possible (from liquid helium temperature to 103 K). In addition, the presence of superparamagnetic particles in the systems under study requires high magnetic field strengths (to 100 kŒ or 1.26×10^{-9} A m^{-1}). Some difficulties in the design of multipurpose instruments are due to the need for meeting all requirements listed above.

Static methods are based on the Faraday method and widely used for paramagnetic susceptibility measurements.[10,11] In the Faraday method, a sample is placed in a region of a constant magnetic field gradient which can be determined upon calibration using the sample with known magnetization. Usually, the force acting on the sample is measured,

$$F = \chi V H \frac{\mathrm{d}H}{\mathrm{d}x}, \qquad (1)$$

where χ is the magnetic susceptibility, V is the sample volume, H is the magnetic field strength and $\mathrm{d}H/\mathrm{d}x$ is the gradient of the magnetic field strength with respect to the x axis. This axis can be oriented either vertically (Faraday balance) or horizontally (pendulum balance).

Usually, there is a small region of constant magnetic field gradient between the poles. Since it is undesired that the sample be in magnetic fields with strongly different strengths, small samples are used. The Faraday method is particularly convenient in the studies of the dependences of the magnetization on the magnetic field strength in a wide temperature range.

There are some severe restrictions on the Faraday method. One of them is that the magnetization is never measured in a true uniform field because the force measurements require a field gradient at a finite distance. For all substances whose magnetic moments depend on the magnetic field strength (*i.e*., ferro- and ferrimagnetics), this restriction may be essential. In addition, investigations of processes accompanied by changes in the magnetization as a result of a chemical reaction face hardware difficulties due to a large 'dead' volume of the instrument.

Dynamic methods involve measurements of the potential created in coils placed in a magnetic field when the sample moves near the coils. The potential is proportional to the magnetic moment of the sample. The most widely used method is the Weiss extraction technique.[12] A sample is placed in a uniform field between the poles of a magnet. Two pairs of Helmholtz coils connected to the data acquisition and processing unit are arranged on both sides of the sample. At the instant of measurements, the sample is rapidly moved 'up' in such a manner that it still be in a uniform magnetic field. As a result, an electric potential proportional to the magnetization of the sample is induced in the coils. Data processing systems in modern instruments integrate signals from a series of motions, which improves the accuracy of measurements. Also, superconducting solenoids are used, which allow one to produce rather high field strengths.

Yet another dynamic method is the Foner technique involving a vibrating magnetometer. In this case, a high-precision oscillator induces acoustic oscillations of the sample in the direction perpendicular to the applied field. The voltage induced in the detecting coils is proportional to the magnetization of the sample. In essence, the Weiss method differs from the Foner technique only in the data processing system.[13] Unlike the extraction magnetometer, in the vibrating magnetometer the signal from the coils is phase detected and then amplified. The method offers great prospects for studying catalysts containing a ferro- or ferrimagnetic phase.[14] Some difficulties appear only in studies of conductors because eddy currents are induced. However, in most cases metal particles are electrically insulated from one another so there are no eddy currents. In spite of clearly seen advantages, the method is still of limited use.

The vibrating magnetometer method appeared to be highly informative in studies of catalysts containing ferromagnetic metals (Fe, Co, Ni).[15,16] A sample of a catalyst of mass 1 to 50 mg was immobilized between two gas-permeable membranes made of porous quartz in a quartz flow microreactor which simultaneously served as a measuring cell of the vibrating magnetometer. Such a design of the magnetometer allows one to record all chemical processes accompanied by changes in the magnetization of the substance under study. Figure 1 presents a schematic of a vibrating magnetometer for *in situ* studies of supported catalysts.

The method allows one to investigate topochemical reactions of ferromagnetic components of catalysts in both isothermal and temperature-programmed regimes in a controllable gas medium in the temperature range from room temperature to 1000 K. A key advantage of the method consists in that the temperature-programmed reduction or oxidation (TPR and TPO, respectively), as well as the surface reaction can be stopped at any instant by replacing the reaction medium by an inert gas and to measure the magnetic properties. Having known the magnetic properties, one can obtain information on the proportion of the metallic phase and in some cases on the size and size distribution of metal particles.

This offers great prospects for *in situ* investigations of topochemical reactions proceeding both in the stage of catalyst preparation and in the course of the catalytic reaction. A combination of traditionally used temperature-programmed reduction with continuous magnetization measurements made it possible to obtain basically new

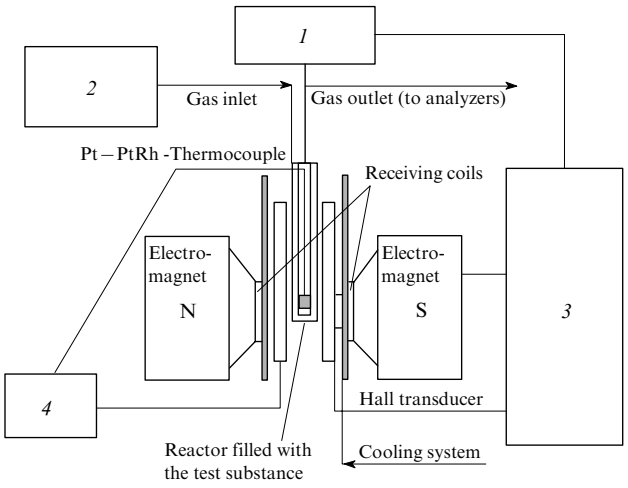


Figure 1. Schematic of a vibrating magnetometer for *in situ* studies of supported catalysts.
Mechanical oscillator (*1*); gas purification system, flow rate and pressure control (*2*); magnetic field control system, signal acquisition and processing unit (*3*); and the heating or cryostat control system (*4*).

information on the topochemical processes that accompany the reduction, oxidation or some other reaction in supported catalysts. The potential of magnetic methods will be illustrated below.

III. Single-domain and superparamagnetic metal particles

Since metal nanoparticles exhibit specific physical properties, we ill consider the magnetic properties of small ferromagnets in more detail.[17]

The domain structure of a bulk ferromagnet appears as a result of minimization of the total energy including:

— the exchange energy (it is minimum when electron spins are aligned in the same direction);

— the energy of crystallographic anisotropy (it is due to the existence of the 'easy' and 'hard' magnetization axes in the crystal),

— the magnetostatic energy due to the existence of magnetic poles inside and on the surface of the sample, and

— the magnetostrictive energy due to the 'tendency' of the domains to change their lengths.

The closure of the magnetic fluxes of the domains reduces the number of magnetic poles within the sample and, as a consequence, the magnetostatic energy. Ferromagnetic domains, *i.e.*, regions with spontaneous saturation magnetization, mainly align to the 'easy' magnetization axis. Frenkel and Dorfman[18] were the first who predicted that sufficiently small ferromagnetic particles should become single-domain ones. Indeed, a decrease in the particle diameter causes the magnetostatic energy (proportional to the volume) to decrease faster than the interdomain boundary energy (proportional to the surface area). Kondorsii developed a rigorous single-domain concept,[19, 20] according to which the limiting, or critical, particle radius (R_c) at which uniform magnetization still persists, is given by

$$R_c \approx \frac{0.95}{J_s}\,(10\times A)^{1/2}\left(Q-\frac{2K}{J_s^2}-\frac{H}{J_s}\right)^{-1/2}, \qquad (2)$$

where J_s is the saturation magnetization, A is the exchange energy parameter, Q is the demagnetization factor, K is the anisotropy constant and H is the magnetic field strength. Note that a particle whose radius meets the condition (2) remains single-domain at all $H > -2K/J_s$. The strict single-domain condition has the form

$$R < R_c \approx \frac{0.95}{J_s}\left(\frac{10\times cB}{a_0 Q_R}\right)^{1/2}, \qquad (3)$$

where $c = 1/2$, 1 and 2 for the simple cubic, body-centred cubic and face-centred cubic lattices, respectively; $B = z^2A$ is the exchange energy parameter; z is the number of uncompensated spins per atom; A is the exchange integral; a_0 is the lattice constant and Q_R is the demagnetization factor of the single-domain ellipsoid along the short axis.

Substitution of numerical values of these parameters into Eqn (3) gives the maximum critical radius of single-domain particles. The determination of the critical size of single-domain particles was debated in reviews (see, *e.g.*, Refs 21 and 22). The critical diameters (D_c) of spherical single-domain particles are as follows:[23]

Material	Co	Fe	Ni	Fe_2O_3	γ-Fe_2O_3
D_c/nm	20	14	55	128	166

As ferromagnetic particles approach the single-domain state, coherent rotation of most individual atomic magnetic moments becomes the main remagnetization mechanism. This is precluded by the crystallographic anisotropy and shape anisotropy. Remagnetization of a spherical single-domain particle by coherent rotation requires that a reverse field be applied

$$H_{c\,max} = \frac{2K_e}{J_s}, \qquad (4)$$

where $H_{c\,max}$ is the maximum coercive force and K_e is the effective anisotropy constant. The dependence of the coercive force on the particle size has been studied for long by different authors.[24, 25] Such a dependence was obtained[25] for the systems comprising iron nanoparticles supported on silica gel or alumina. A qualitative diagram is shown in Fig. 2.

As D decreases to D_c, the existence of domain walls becomes energetically unfavourable and the particle turns single-domain. It is noteworthy that a critical-size single-domain particle is characterized by the maximum coercive force because its magnetization can no longer change due to the motion of the domain walls; a coherent spin rotation is required instead.

A single-domain particle retains its uniform magnetization as the particle size decreases, because the vectors of the atomic moments are held parallel to one another through exchange coupling. However, a decrease in the particle volume makes a kind of Brownian motion of the vector of the total magnetic moment

$$\mathbf{M} = V J_s$$

more probable.

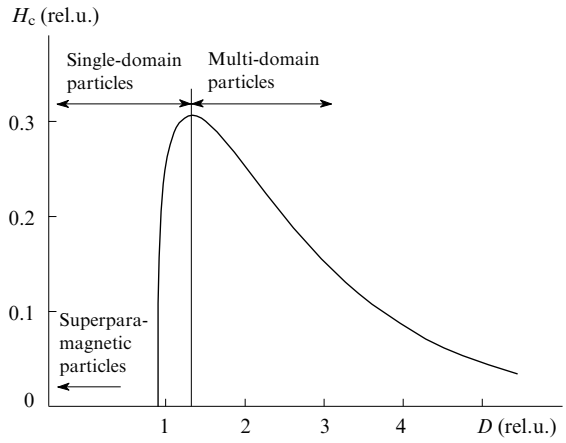


Figure 2. Dependence of coercive force on the cobalt and iron particle size.

Thermally induced fluctuations can cause rotation of the vector **M** only upon the overcoming of an energy barrier E. The probability of such a process is proportional to $\exp(-E/k_B T)$, where k_B is the Boltzmann constant. The total magnetization of an ensemble of N particles

$$J = N\mathbf{M},$$

in the field H tends to zero after switching off this field owing to Brownian motion of the orientations of the magnetic moment vectors of individual particles as follows:

$$J = J_s \exp\left(-\frac{t}{\tau}\right), \tag{5}$$

where t is the running time and τ is the relaxation time. Thus, the system of small particles behaves like an ensemble of paramagnetic atoms having large magnetic moments. This phenomenon called superparamagnetism was studied theoretically[26] and experimentally.[27,28] It is assumed that the relaxation time τ depends on the energy barrier E

$$\tau = \tau_0 \exp\left(\frac{E}{k_B T}\right), \tag{6}$$

where the parameter τ_0 varies from 10^{-9} to 10^{-10} s;

$$E = KV,$$

i.e., the energy depends on the anisotropy constant and the particle volume. According to expression (6), τ depends on both V and T.

Particles exhibit superparamagnetic properties if their diameters become smaller than the critical diameter. In essence, superparamagnetism is a specific kind of ferromagnetism corresponding to a thermodynamic equilibrium between the magnetic moment of the particle, magnetic field and temperature. As a result, superparamagnetic materials show no stable residual magnetization. Therefore, to gain a better insight into these phenomena, we will consider particles whose diameters are no less than D_c, ferromagnetic particles and particles whose diameters are no more than D_c. However, one should keep in mind that D_c depends on the temperature at which the measurements are carried out [see expression (6)].

Strictly speaking, we should consider the so-called blockage temperature (T_b), or the blocked state of magnetic moments. The blocked state corresponds to the temperatures below T_b, at which the system has no time to approach the equilibrium state during the measurement time. As a result, some blockage effects will manifest themselves in the magnetic properties of the system. For instance, in the case of magnetostatic measurements with magnetic field reversal, the remagnetization curves will show the coercive force and residual magnetization. The blockage temperature is measured by cooling the system under study in a magnetic field (FC) and in a zero magnetic field (ZFC). On subsequent heating in a weak magnetic field, the field dependences of magnetization plotted after FC and ZFC should match each other at the blockage temperature. At temperature above T_b, the system is characterized by a short relaxation time (compared to the measurement time) and at each experimental point it has time to approach the equilibrium state corresponding to this point. As a result, the blockage effects will almost not manifest themselves. The T_b value will strongly depend on the measurement time characteristic of each experiment.

Assuming that $\tau_0 = 10^{-9}$ s, one can easily determine the critical parameters of superparamagnetism for different metals. For instance, the relaxation time of iron particles 30 nm in diameter at 300 K is 4×10^6 s, being $\sim 6 \times 10^{-2}$ s as the particle volume is halved ($D_c = 23.8$ nm). This result can also be obtained upon raising the temperature to 600 K. Thus, at room temperature, particles with diameters 23.8 nm or smaller will attain thermal equilibrium after a few hundredth of a second and, therefore, manifest superparamagnetic properties. At the same time, 30-nm iron particles are very stable at room temperature; they will behave as single-domain ferromagnets. Particular type of the behaviour of the system of small particles depends on the time necessary to change the magnetic properties. Usually, this time is set equal to 100 s for static measurements; then, transition to the superparamagnetic state occurs provided that

$$KV = 25 k_B T,$$

where T is the measurement temperature. If $V \geqslant 25 k_B T/K$, one deals with single-domain particles; if $V \leqslant 25 k_B T/K$, particles exhibit the properties of a superparamagnetic.

When placed in an external magnetic field H, particles acquire an additional energy which changes the energy barrier E and, therefore, the relaxation time. The expression for the coercive force H_c or the reverse field necessary for thermal fluctuations to disorient the vectors **M** of particles of volume V within 100 s has the form[29]

$$H_c = \frac{2K}{J_s}\left[1 - 7\left(\frac{k_B - BT}{KD_c^3}\right)^{1/2}\right]. \tag{7}$$

At $T = 0$ K, one has

$$H_0 = \frac{2K}{J_s},$$

while at $T = KV/25 k_B$, one gets $H_c = 0$. Using Eqn (7), one can determine the critical volume (V_c) by extrapolating the

measured size dependence $H_c(D_c)$ to $H_c = 0$ and then calculating the quantity $2K/J_s$.

However, one should keep in mind that the anisotropy constant also depends on the particle size.[30] According to a core–shell theory,[31] the parameter K should be calculated with inclusion of the contribution of the surface atoms to the anisotropy. Clearly, this contribution increases with an increase in the ratio of the number of surface atoms to the total number of atoms in the particle. It was assumed [32] that the energies E of the systems comprised of ultradisperse particles depend solely on their surface areas rather than volumes.

When the anisotropy effects are negligible ($k_BT \gg KV$), the magnetization vectors of individual particles randomly change their orientations under the action of thermal fluctuations. This is accompanied by disappearance of the indications of ferromagnetism. The hysteresis loop degenerates to a single sigmoidal curve, *i.e.*, the coercive force and the residual magnetization become equal to zero. In this case, the dependence of magnetization on the external magnetic field is given by the Langevin expression

$$J = J_s\left(\mathrm{cth}\frac{MH}{k_BT} - \frac{k_BT}{MH}\right). \quad (8)$$

Having expanded the hyperbolic cotangent into a series, one gets at $MH \gg k_BT$

$$J \approx J_s\left(1 - \frac{k_BT}{MH}\right). \quad (9)$$

At $MH \ll k_BT$, one has

$$J \approx J_s\frac{MH}{3k_BT}. \quad (10)$$

If the particle size distribution is given by the function $f(V)\mathrm{d}V$, the total magnetization of the sample volume V_0 is

$$J = J_sV_0\int_0^\infty\left(\mathrm{cth}\frac{J_sVH}{k_BT} - \frac{k_BT}{J_sVH}\right)f(V)\mathrm{d}V. \quad (11)$$

Expression (11) makes it possible to determine the particle size distribution from the dependence of magnetization on the magnetic field strength. From Eqn (11) it also follows that the field dependences measured at different temperatures should match one another in the coordinates $J-H/T$. A distinctive feature of the superparamagnetic behaviour of an ensemble of particles is the close space between the magnetization curves plotted in the coordinates mentioned above.

IV. Magnetic granulometry methods

Since the average size of metal particles and the particle size distribution are of paramount importance for supported catalysts, now we will dwell on the methodology of magnetic granulometry in more detail. As mentioned above, Eqns (9)–(11) allow one to determine the average particle size and the particle size distribution $f(D)$. At low field strengths (small H/T ratios), from Eqn (10) one can derive the following expression for the particle size:

$$D_1 = \left[\left(\frac{J}{H}\right)\left(\frac{18k_BT}{\pi\rho J_s^2}\right)\right]^{1/3}, \quad (12)$$

where ρ is the density of the metal.

For strong fields, from Eqn (9) one gets

$$D_2 = \left[\frac{6k_BT}{(J_s - J)\pi\rho H}\right]^{1/3}. \quad (13)$$

Since at $H \to 0$ the dependence of the magnetization on the field strength is 'sensitive' to the presence of large particles, expression (12) estimates the upper bound of the particle size. Correspondingly, in strong fields, the approach to the saturation magnetization is mainly controlled by the small particles present in the sample; therefore, relation (13) specifies the lower bound of the particle size. Expressions (12) and (13) are widely used for the determination of the particle size of Ni-supported catalysts.[33–35]

A method [7] for the determination of the particle size distribution uses the Langevin function $L(n,H)$ and Eqn (11) has the form

$$\frac{J}{J_s} = \sum_{n=0}^{\infty} g(n)\,L(n,H,), \quad (14)$$

where n is the chosen interval of D and $g(n)$ and $L(n,H)$ are the average $f(D)$ and $L(D,H)$ values on the specified interval. One can obtain the system of equations for some given field strength values H_i

$$\left(\frac{J}{J_s}\right)_{H_1} - g(D_1)\,L(D_1,H_1) + g(D_2)\,L(D_2,H_1) + \ldots = y_1, \quad (15)$$

$$\left(\frac{J}{J_s}\right)_{H_2} - g(D_1)\,L(D_1,H_2) + g(D_2)\,L(D_2,H_2) + \ldots = y_2.$$

The system of equations (15) can be solved with respect to $g(D_i)$ using conventional software based on Marquardt's adaptation of the Newton–Raphson algorithm. The initial $g(D_i)$ values necessary for the iterative procedure are determined from the condition for minimum of the quantity

$$Q = \sum_n y_n^2.$$

A lognormal distribution function is used as the initial approximation.

The method works well even for the bimodal distributions.[36] However, one should keep in mind that, generally, the final result depends on the shape of the initial distribution. In essence, here we have to solve the inverse problem, which is well known in physics and physical chemistry. It should be emphasized that practical implementation of this method requires the use of rather high field strengths (to 100 Œ), which can be reached only with superconducting solenoids. The stronger the magnetic field the higher the accuracy of determination of J_s because in this case the saturation magnetization is determined by extrapolating the magnetization curve to H_∞. In addition, an exact determination of J_s requires that the measurements be carried out at liquid helium temperatures. If the particles size is less than 2 nm, the determination of J_s is a specific complicated task.

Potton *et al.*[37] proposed a technique to avoid these difficulties using the maximum entropy (S) method including an algorithm reported by Skilling and Bryan.[38] The maximum entropy method allows this type of problems to be solved without specifying the initial pattern of the particle size distribution. It uses all experimental data including the errors of particular measurements. The essence of the method is to search for the maximum value of the expression

$$S = -\sum_{j=1}^{N} f_j \ln\left(\frac{f_j}{b_j}\right), \tag{16}$$

where f_j is the distribution function, b_j is the initial value of the parameter P

$$P = \sum_{i=1}^{P} \frac{(J_i/J_s - y_i)}{\sigma_i^2}, \tag{17}$$

where summation is performed over the number of measurements at a given point; here σ_i^2 is the dispersion at each point and the quantities J_i and y_i are determined from the system of equations (15).

Thus, solution of the system (15) requires a physical model which is included in the Langevin equation and the measured values of the magnetization at a given field strength. It is not necessary to specify the initial particle size distribution f and the J_s value. The last-mentioned parameter can be determined using the normalization condition for the function f. The maximum entropy method was successfully used[39] to determine the size distribution function of nickel particles in the Ag–Ni alloy. It is very efficient in the analysis of the bimodal distribution.[40] Also, the Potton technique was employed to construct the particle size distribution for Co/SiO_2 catalysts.

Yet another approach to the studies of the particle size distribution was first proposed by Weil.[41] It is based on measurements of the temperature dependence of the residual magnetization. At a preset temperature, the residual magnetization should be a measure of the amount of the substance whose particle volumes are larger than the critical volume. Weil used his method to investigate nickel powder and established a bimodal particle size distribution which was explained by specific features of the powder preparation procedure. However, this technique is of limited use.

Recently, methods using the so-called genetic algorithm become increasingly more popular. Various methods for construction of the size distribution of metal particles were compared.[42] They included a conventional technique using the Langevin equation [system of equations (15)], the Monte Calro method as well as methods involving the genetic algorithm. The genetic algorithm is a heuristic search algorithm for solving optimization problems and modelling. It involves random selection, combination and variation of the desired parameters using mechanisms similar to the biological evolutionary ones. A distinctive feature of the genetic algorithm is the use of a 'crossing' operator responsible for the recombination of candidate solutions; the role of this operation is similar to that of crossing in living nature.[43]

All methods for constructing the particle size distributions (see above) were developed assuming uncorrelated behaviour of particles. However, in real systems the expected pattern may be significanly distorted owing to interparticle interactions. This first of all manifests itself in mismatch of the magnetization curves measured at different temperatures and plotted in the $J-H/T$ coordinates.

Here researchers deal with the problem of interparticle interactions, which significantly complicates the situation or makes it almost insoluble. In each particular case one can calculate some limiting values of parameters at which the problem can be solved within the framework of the theories outlined above. There are dipole–dipole interactions between individual superparamagnetic particles. The energy of the dipole–dipole interaction between particles having the magnetic moment M can be estimated using the following approximate expression[44]

$$E_{int} = \frac{M}{l^3},$$

where l is the interparticle distance. For a system of superparamagnetic particles 10 nm in diameter (D) separated from one another by a distance of 2 D from the relation

$$E_{int} = k_B T$$

it follows that the temperature of transition to the ordered state is ~ 300 K.

Consider a system of N spherical superparamagnetic particles with the average radius R, arranged on the surface of a porous support with the pore volume V_p. Based on general physical considerations, suppose a Poisson distribution of metal particles over the support surface. Then the distribution function of the distances between the centres of particles is given by[45]

$$f(l) = 4\pi l^2 \lambda \exp\left(-\lambda \frac{4}{3}\pi l^3\right), \tag{18}$$

where $\lambda = N/V_p$ is the number of metal particles per unit volume of the porous support. The average distance between the particles is

$$\overline{l} = 4\pi\lambda \int_0^\infty l^3 \exp\left(-\lambda \frac{4}{3}\pi l^3\right) \mathrm{d}l. \tag{19}$$

After integration one gets

$$\overline{l} \approx 0.55\left(\frac{V_p}{N}\right)^{1/3},$$

and therefore,

$$E_{int} \approx \frac{0.17MN}{V_p}.$$

This expression allows one to calculate the energy of dipole–dipole interaction for a particular supported catalytic system.

The magnetic granulometry method (see above) is only applicable to an ensemble of superparamagnetic particles. Construction of distribution functions for systems containing single-domain particles is much more complicated.

If the system contains no multi-domain particles, the particle size distribution can be analyzed using the equation[28]

$$\gamma = 1 - \frac{2J_r}{J_s}, \tag{20}$$

where γ is the proportion of superparamagnetic particles and J_r is the residual magnetization. The upper bound of the size of superparamagnetic particles at room temperature can be estimated from the relation

$$KV = 25 k_B T, \tag{21}$$

where K is the anisotropy constant (for the cobalt face-centred lattice, $K = 5 \times 10^6$ erg cm^{-3}).[30] The largest diameter of superparamagnetic particles which fulfills Eqn (21) at 283 K (measurement temperature) is $\sim$7.6 nm. The anisotropy constant depends on the type of the crystal lattice.[46]

Application of magnetometric methods for the determination of the particle size is correct only provided that the magnetic system contains no multi-domain particles. For cobalt, these are particles larger than 20 nm.[47] Thus, prior to measurements one should ensure that the systems under study comprise only single-domain particles. This can be done using a procedure developed to study Co-supported catalysts.[48] Following this procedure, reduced catalysts were slightly oxidized at room temperature and the coercive force was measured before and after the oxidation. If the system contains multi-domain particles, H_c after oxidation; otherwise, if the system is free from multi-domain particles, H_c decreases (see Fig. 2).

A method of granulometric analysis based on the hysteresis loop was proposed.[49] The magnetic field dependence for a system containing cobalt particles is shown in Fig. 3. The system Co/MgO–Al_2O_3 contains two types of cobalt particles, *viz*., large single-domain particles responsible for the residual magnetization (J_r) and small superparamagnetic particles responsible for the lack of saturation in high fields ($H > 8000$ Œ).

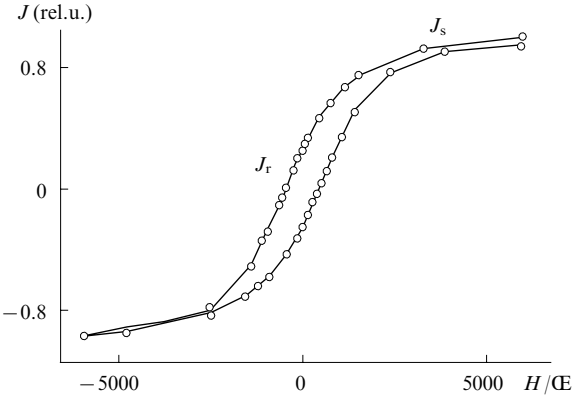


Figure 3. Magnetic field dependence for a system containing cobalt particles.[50]

The behaviour of superparamagnetic particles in the magnetic field is described by the Langevin function.[51] The distribution of large particles is calculated assuming a spherical shape and uniaxial anisotropy of single-domain particles. The large ferromagnetic particles are described in the framework of the known Stoner–Wohlfahrt model for single-domain particles with uniaxial magnetocrystalline anisotropy and 'easy' magnetization axis.[24]

The proportions (by mass) of the superparamagnetic and single-domain components of the distribution (α and β, respectively) were determined after normalization assuming that the volumes of the two fractions of particles are proportional to their saturation magnetization

$$\alpha + \beta = 1, \tag{22}$$

$$\frac{\alpha V_1}{\beta V_2} = \frac{M_s^{(1)}}{M_s^{(2)}},$$

where V_1 and V_2 are the volumes and $M_s^{(1)}$ and $M_s^{(2)}$ are the magnetizations of the corresponding fractions (reference data for bulk metals).

The magnetic moment of a cobalt atom is 1.62 μ_B and the cobalt face-centred cubic lattice is characterized by $a = 3.545$ Å. Calculations give the following values: $M_s = 1349$ Œ cm^{-3}, uniaxial anisotropy constant $K_1 = 4.53 \times 10^6$ erg cm^{-3} (at $H_0 = 3358$ Œ) and the exchange interaction constant $A = 2.8 \times 10^{-6}$ erg cm^{-1} (experimental value for cobalt nanocrystals).[52] In this case, the ferromagnetic exchange length is 78.6 Å. The calculated particle size distribution is shown in Fig. 4.

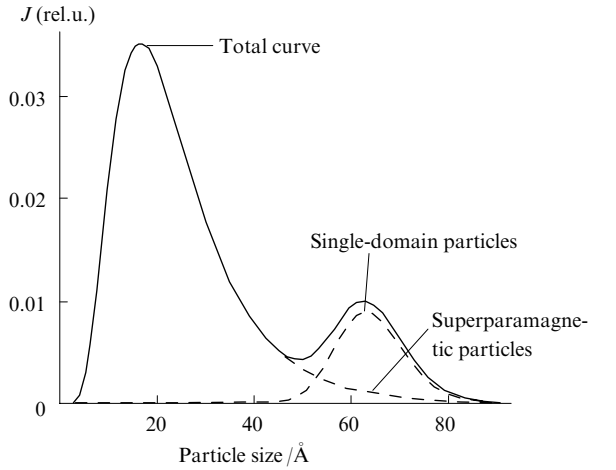


Figure 4. The size distribution of cobalt particles.

The temperature dependence of the residual magnetization allows the particle size distribution in a catalyst containing single-domain and superparamagnetic particles to be calculated in another manner. Assume a lognormal distribution; then, its shape is determined by two parameters, namely, the average value and dispersion. The results of magnetic measurements characterize the particle volumes or, in essence, the particle volume distribution.

The upper bound of the single-domain region depends only slightly on temperature at least in the interval from 293 to 373 K corresponding to magnetic measurements.[53]

Taking into account Eqn (20) and assuming the lognormal distribution, one can write the following system of equations:[54]

$$\gamma_1 = 1 - \int_{V(T_1)}^{V_{20}} F(V;\mu,\sigma)\mathrm{d}V \Big/ \int_0^{V_{20}} F(V;\mu,\sigma)\mathrm{d}V, \tag{23}$$

$$\gamma_2 = 1 - \int_{V(T_2)}^{V_{20}} F(V;\mu,\sigma)\mathrm{d}V \Big/ \int_0^{V_{20}} F(V;\mu,\sigma)\mathrm{d}V,$$

where $V(T_i)$ is the critical volume of the superparamagnetic particle at the temperature T_i calculated from Eqn (21), V_{20} is the volume of a particle 20 nm in diameter, and

$$F(V;\mu,\sigma) = \frac{1}{V\sigma\sqrt{2\pi}} \exp\left[-\frac{(\ln V - \mu)^2}{2\sigma^2}\right]$$

is the probability density of the lognormal distribution.

The system of equations (23) can be numerically solved with respect to the unknown parameters μ and σ; this allows one to determine the average value and the root-mean-square deviation of the particle volume

$$\bar{V} = \exp\left(\mu + \frac{\sigma^2}{2}\right), \qquad (24)$$

$$\overline{(V - \bar{V})^2} = \exp Big(2\mu + 2\sigma^2) - \exp\left(2\mu + \sigma^2\right).$$

Thus, having measured the magnetic field dependences of the magnetization at two temperatures, one can calculate the parameters of the lognormal distribution.

Good agreement between the average sizes of cobalt particles obtained by the magnetometric method and by TEM is illustrated in Fig. 5.[55]

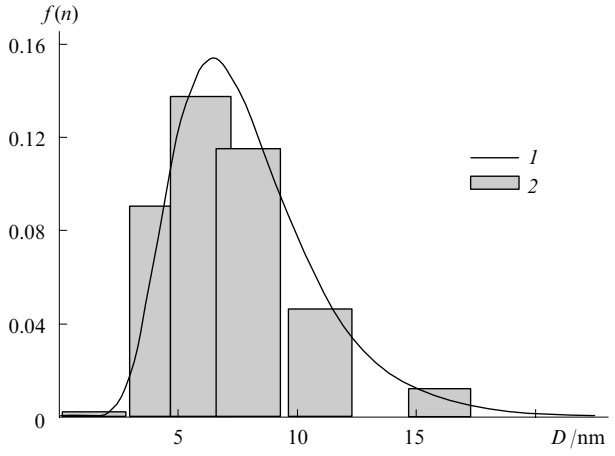


Figure 5. The cobalt particle-size distributions obtained by the magnetometric method (*1*) and by TEM (*2*).

V. Magnetization of metal particles and adsorption of molecules from the gas phase on them

The magnetic properties discussed above are mainly characteristic of bulk ferromagnets. Clearly, as the particle size decreases, the contribution of surface atoms having a lower coordination number to the properties in question increases. The surface atoms of a magnet adsorb gas molecules; the metal d-orbitals are involved in the bonding to adsorbate and no longer participate in exchange interaction. After adsorption of gas molecules, the surface atoms do not contribute to the total magnetization of the particle. In studies of the magnetic properties of small ferromagnets (especially when investigating topochemical reactions of ferromagnetic nanoparticles) one should take into account the influence of adsorption on their magnetization.

This effect is most pronounced in the case of adsorption on nickel. Supported nickel catalysts are characterized by a reversible linear dependence of the magnetization on the degree of coverage of the surface with hydrogen (so-called magnetic isotherm). The slope of the isotherm (α_{H_2}) expressed in Bohr magnetons per adsorbed molecule is about 1.4. The magnetic moment of a nickel atom (μ_{Ni}) is 0.6 μ_B; therefore, $\alpha_{H_2} \approx 2\,\mu_{Ni}$. It follows that nearly two nickel atoms are excluded from the magnetic interaction under the conditions of dissociative adsorption of hydrogen on nickel.

In the case of supported Co catalysts, the dependence of the magnetization on the degree of surface coverage with hydrogen is much more complicated. For nickel, the dependence of the relative change in the magnetization on the degree of coverage of the surface with hydrogen is temperature independent. Contrary to this, for cobalt the quantity α_{H_2} increases with temperature, thus indicating an activated character of hydrogen adsorption on cobalt.[56] The assumption that hydrogen adsorption on cobalt catalysts is an activated process was first reported by Zowtiak and Bartholomew.[57] A decrease in the magnetic moment of cobalt upon adsorption of hydrogen at 300 K is 0.54 ± 0.06 μ_B per atom or $\alpha_{H_2} \approx 1$.[58] More detailed studies revealed two types of hydrogen chemisorption on cobalt, *viz*., molecular adsorption at room temperature ($\alpha_{H_2} \approx 0.3$ μ_B) and dissociative adsorption at 200 °C ($\alpha_{H_2} \approx 0.7$ μ_B).[59] The situation for cobalt is as follows: if, as for nickel, the magnetic component does not contribute to the adsorption on the surface atoms, the α_{H_2} values are much lower than those expected from the calculations based on the magnetic moment of cobalt atom (1.6 μ_B). Under identical conditions, this implies no coverage of the surface of metallic cobalt with hydrogen.

Thus, hydrogen adsorption is not a preferred method for measuring the degree of dispersion of cobalt. This provides an explanation for the interest in magnetic granulometry methods for characterization of Co-containing catalysts. A comparison of H_2 and O_2 adsorption on NiCu showed[56] that, unlike oxygen, hydrogen does not react with the surface atoms (*i.e*., no hydride is formed); in the presence of hydrogen one deals with magnetic disordering of the surface atoms.

In the case of hydrogen adsorption on highly disperse iron, the magnetization shows no decrease within the limits of experimental error. This can be to some extent due to the difficulty to achieve a high degree of iron reduction.[60] Hydrogen adsorption on ultradisperse iron has no effect on the magnetization within the limits of experimental error ($\alpha_{H_2} \approx 0$ μ_B).[61] Clearly, α_{H_2} decreases in the order

Ni > Co > Fe.

This is due to different electronic structures of these metals, which vary from the 'magnetically hard' ferromagnetic structure of nickel (the Fermi level crosses only the d↓-sublevel) to the 'magnetically soft' structure of iron (Fermi level crosses both d↓-level and d↓-sublevels). Hydrogen adsorption causes changes in the population of the Fermi level, *viz*., one deals with strong perturbations when considering only one sublevel (Ni) and with considerable changes in the magnetization when considering two sublevels (Fe); cobalt occupies an intermediate position.[62]

Comprehensive information on adsorption of other substances was reported in a monograph.[6] The number of

surface atoms magnetically disordered upon adsorption was called the magnetic bond number.[6,8] This term is particularly convenient when studying nickel catalysts. It was extended to a number of molecules that are structurally similar to the corresponding adsorbates and confirmed by IR spectroscopy and by the results of magnetic measurements during CO adsorption on NiCu.[63]

Now we will briefly outline the results obtained in our studies of Ni- and Co-supported catalysts for CO hydrogenation with a vibrating magnetometer. Figure 6 presents the plot of the magnetization *vs.* number of CO portions (volumes) passed through the catalyst 40 mass % Ni/SiO_2 at 300 K. Carbon monoxide was supplied portionwise (0.05 cm^3 CO per portion) *via* a loop injector in argon stream and detected at the reactor outlet by an IR detector. After supply of each CO portion the magnetization initially decreased and then increased to some extent. This is probably due to partial desorption of CO after switching from carbon monoxide to argon. After the seventh portion, a partial 'slip' of CO was observed, thus indicating an approach to the equilibrium coverage.

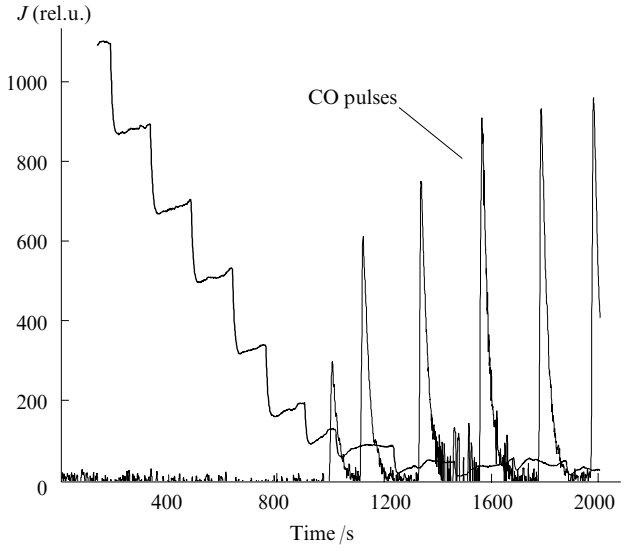


Figure 6. Magnetization plotted *vs.* number of CO pulses passing through the catalyst 40 mass % Ni/SiO_2 at 300 K.

A ferromagnetic resonance study[64] of the effect of CO adsorption on cobalt nanoparticles showed that the resonance line weakens but does not disappear upon CO adsorption.

Processes detected during oxygen adsorption on nickel or cobalt at 283 K should most probably be treated as the reactions of low-temperature oxidation (see below).

Changes in the magnetization of the catalyst Ni/Cr_2O_3 on going from hydrogen to argon stream and *vice versa* at 400 K are illustrated in Fig. 7. The observed increase in the magnetization upon 'switching' from hydrogen to argon can mainly be due to the desorption of hydrogen; subsequent back-'switching' causes a fast decrease in the magnetization to the value observed in the hydrogen stream. Taking into account these results, magnetic measurements using freshly reduced catalysts should be carried out after preliminary desorption of hydrogen.

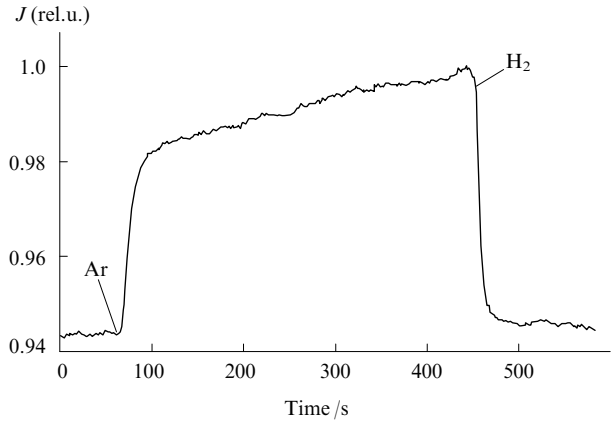


Figure 7. Changes in the magnetization of the catalyst Ni/Cr_2O_3 upon replacement of hydrogen flow by argon flow and *vice versa* at 400 K.

VI. Supported catalysts as systems of nanoparticles

Since supported catalysts represent systems of nanoparticles distributed in porous supports, it seems appropriate to dwell on some unusual chemical properties of these objects. Unusual character of these properties is due to the so-called size effects, a feature of the particles whose size is comparable with or smaller than the characteristic length used in a certain macroscopic theory. Such effects are well known in physics of small particles[65] and in chemistry of nanoparticles. There is considerable literature on the subject including a comprehensive review[66] of the most important results. However, it should be noted that most studies are devoted to particles comprised of $\leqslant 10^2$ atoms (*i.e.*, the particle size is at most 1–2 nm), whereas metal particles in supported catalysts are usually much larger (5 to 100 nm in size). Topochemical reactions occurring during the preparation of such catalytic systems and accompanying catalytic reactions, *e.g.*, reduction and oxidation of metal nanoparticles, are of particular interest.

Studies on the size effects in topochemical reactions involving metal nanoparticles in supported catalysts are scarce.

The lower bound of the size of metal particles can be determined from the following considerations. The separation between the electron energy levels (δ) in a metal particle is given by

$$\delta \approx \frac{\varepsilon_F}{N},$$

where ε_F is the Fermi level and N is the number of atoms in the particle. Estimation of the N value assuming that $\delta = 2.5 \times 10^{-2}$ eV and $\varepsilon_F \approx 10$ eV at room temperature gives $N \approx 400$ or 2 nm for the corresponding particle size; at smaller particle size, the metallic properties weaken.

Determination of the upper bound of the particle size is ambiguous and depends on which processes occurring in the system are treated as size-dependent ones. Metal particles in supported catalysts contact the reaction medium and the support; therefore, topochemical reactions at metal/support and metal/reaction medium interfaces should first of all be considered as size-dependent processes.

Specific features of chemistry of nanoparticles are due to at least two factors, namely, thermodynamics of small particles and the kinetics of reactions involving them.

A small particle can be treated as a 'thermodynamic phase'; however, the additivity of its properties with respect to the number of constituent atoms is violated owing to a large proportion of surface atoms. Because of this, rigorous classification of thermodynamic parameters into extensive and intensive ones is no longer valid. For instance, small particles are characterized by two (differential[67] and integral) chemical potentials given by

$$\mu = \frac{\partial G}{\partial N}$$

and

$$\hat{\mu} = \frac{G}{N},$$

respectively, where G is the Gibbs thermodynamic potential where

$$\hat{\mu} - \mu \propto N^{-1/3}.$$

Nanoparticles have an excess free energy compared to bulk materials. Higher energy capacity leads to changes in the phase equilibria in nanoparticles.[68] In addition, changes in the thermodynamic properties of nanoparticles compared to the bulk matter are due to the changes in the shape and position of the phonon spectrum (*i.e.*, the changes in the distribution function of atomic vibrational frequencies), *viz.*, as the particle size decreases, the phonon spectrum is blue shifted, which in turn leads to changes in the specific heat capacity of nanoparticles compared to the bulk phase.[69]

The equilibrium constant for a heterogeneous reaction involving nanoparticles also depends on the particle size because the chemical potential becomes size-dependent.

Numerous examples of the influence of the degree of dispersion on the equilibrium properties are available in the literature (see, *e.g.*, Ref. 70). Therefore, we will dwell on a single aspect of the thermodynamics of nanoparticles which is very important for the purposes of this review. The case in point is the dependence of the thermodynamic reactivity on the particle size.

The degree of dispersion can affect the equilibrium of a chemical reaction

$$-\Delta G_{\mathrm{d}}^{0} = RT \ln \frac{K_{\mathrm{d}}}{K},$$

where $-\Delta G_{\mathrm{d}}^{0}$ is the change in the Gibbs free energy due to the change in the degree of dispersion, R is the universal gas constant, K_{d} is the equilibrium constant of the reaction involving disperse reactants and K is the equilibrium constant for the non-disperse reactants. As the degree of dispersion increases, the activity of reactants also increases and, as a consequence, the equilibrium constant changes.

Consider topochemical reactions in supported catalysts from this point of view. In the simplest case, these include the oxidation of metal nanoparticles and the reduction of oxide.

Assume the occurrence of a reversible reaction

$$M_xO_y + H_2 \rightleftharpoons M_xO_{y-1} + H_2O.$$

In this case, the equilibrium composition of the oxide system depends on the radius of curvature of the interfaces and on the surface energies.[12,71] In particular, in the reduction of small oxide particles, the partial pressure of hydrogen should be higher than the equilibrium pressure characteristic of bulk phases. In other words, each value of the hydrogen partial pressure corresponds to a critical size of the oxide particle such that smaller particles cannot be reduced. Similar results were also obtained by other researchers.[72] We believe that this provides an explanation for a number of experimental facts concerning supported catalysts. For instance, the oxide CoO is formed during CO hydrogenation on Co-supported catalysts at p_{H_2O}/p_{H_2} ratios (p is the partial pressure) at which no cobalt oxide is formed in bulk phases.[73] It follows that the equilibrium constants calculated for bulk systems are not always suitable for the studies of the systems containing small particles (less than 100 nm in diameter) or nanoparticles.

An experimental proof of thermodynamic regularities (see above) was reported.[65] In particular, it was shown that the parameters of the particle size distribution depend on the partial pressure of hydrogen in the course of reduction. Taking into account this fact, the results of TPR studies of catalysts should be interpreted in another manner. Usually, TPR experiments are carried out at relatively low partial pressures of hydrogen ($\sim 5\%$ H_2 in argon, or nearly 37 Torr). The character of the size distribution of cobalt particles affects the shape of the TPR spectrum of the catalyst.[74] The reverse also holds, *i.e.*, the partial pressure of hydrogen used in the TPR experiments influences the size distribution of metal particles. Undoubtedly, this should be taken into account in the TPR studies of supported catalysts. In this case, the activation energies of the reduction of oxide nanoparticles in supported catalysts calculated using the data of non-isothermal TPR experiments can be significantly different from the activation energies determined under isothermal conditions at maximum partial pressures of hydrogen.

VII. Topochemical processes on Fe-containing catalysts

There is considerable literature on the reduction of bulk metal oxides; however, the mechanism of the reduction of supported oxides has been poorly studied. This is due, on the one hand, to the high reactivity of the oxide nanoparticles, and, on the other hand, to the competition between the reduction and the interactions with the support. Detection of the changes in the magnetization during TPR considerably extends our knowledge about the kinetics and mechanism of the reduction of supported oxides.

1. The kinetics of reduction of iron oxides

Supported iron oxides allow one to observe successive reduction[75]

$$Fe_2O_3 \longrightarrow Fe_3O_4 \longrightarrow FeO \longrightarrow Fe.$$

The temperature dependence of magnetization (or the thermomagnetic curve) obtained during programmed heating of the catalyst Fe_2O_3/SiO_2 (12 mass % Fe on KSK-2 silica gel) in hydrogen stream is shown in Fig. 8.[75] Since the temperatures T_1, T_2 and T_3 corresponding to the points A, B and C, respectively, depend on the heating rate, the abscissa axis shows no particular temperature values, except

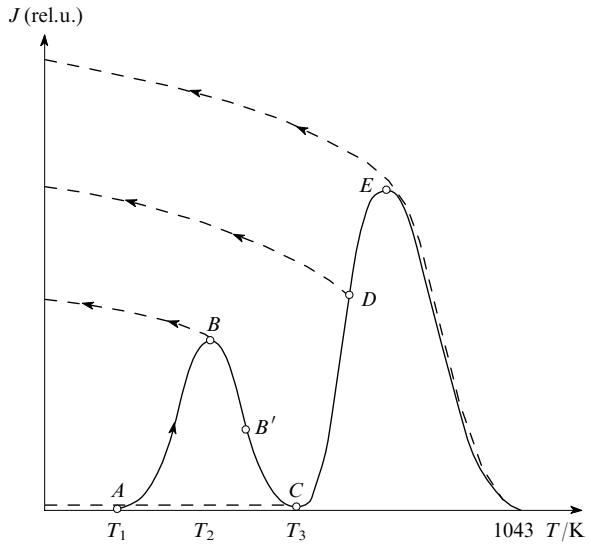


Figure 8. Temperature dependence of magnetization measured in the course of programmed heating of the catalyst Fe_2O_3/SiO_2 in hydrogen stream.

the Curie temperature of iron (1043 K). The thermomagnetic curves obtained on cooling of the sample from a specified temperature to room temperature are shown by dashed lines. An increase in the heating rate causes a shift of the thermomagnetic curve towards higher temperatures; however, as the temperature of 1043 K is reached, the magnetization always vanishes. In particular, it follows that in the range of heating rates used in the experiments (to 1.5 deg s^{-1}), the sample still can attain the thermal equilibrium with the detector (thermocouple).

This experimental procedure allows one to terminate the programmed heating at any instant and either to quench the sample or to continue the experiment in the isothermal regime. It was found that the catalyst sample cooled upon reaching the temperature T_2 represents Fe_3O_4/SiO_2 irrespective of the heating rate. This is indicated by the Curie temperatures of the sample quenched after the temperature T_2 was reached and by the results of powder X-ray diffraction (XRD) and Mössbauer spectroscopy studies. Quenching of the sample after the temperature T_3 revealed that the system also shows no room-temperature magnetization. An XRD and Mössbauer spectroscopy study of the catalyst prepared by cooling from the temperature T_3 showed that iron exists in the form of wüstite (FeO).[76] As the sample is heated above T_3, the increase in the magnetization is due to the FeO reduction to α-Fe, which can be identified with ease in the X-ray diffraction patterns of cooled samples. The method presented above allows one to determine the concentrations of magnetic phases at any point of the thermomagnetic curve.

The total saturation magnetic moment $[M^{(s)}]$ caused by the presence of n magnetic phases that is measured experimentally by a magnetometer is given by

$$M^{(s)}(T) = \sum_i M_i^{(s)}(T), \tag{25}$$

$$M_i^{(s)}(T) = j_i^{(s)}(T)\, m_i, \tag{26}$$

where $j_i^{(s)}(T)$ is the specific saturation magnetization of the ith phase at the temperature T, m_i is the mass of the ith phase, and

$$\lim_{T \to T_C} j_i^{(s)}(T) = 0, \tag{27}$$

where T_C is the Curie temperature of the ith phase. If the functions $j_i^{(s)}(T)$ for each individual phase are known and the experimental values $M^{(s)}(T)$ for n temperatures T are available, one can determine the m_i values from Eqns (25)–(27). It should be noted that this procedure for the determination of the m_i values is valid provided that the contribution of superparamagnetic particles to the magnetization can be neglected. The fact that all samples under study showed magnetic hysteresis[76] suggests that the magnetic subsystem is formed by particles whose size is at least 8 nm.

The specific saturation magnetizations $j_i^{(s)}(T)$ of magnetite and iron were calculated from the experimental dependences of the saturation magnetic moments of the Fe_3O_4 and α-Fe ('chemically pure' grade) samples. To construct the thermomagnetic curves $M^{(s)}(T)$, the sample under study was heated in a stream of thoroughly purified helium to avoid oxidation. The empirical temperature dependences of the specific saturation magnetizations can quite correctly be described by the polynomials $P^k(T)$ (where $k = 7$). By substituting the empirical dependences into the system of equations (25)–(27) one can determine m_i for any point of the thermomagnetic–TPR (TM–TPR) spectrum. As to the relation between the saturation magnetic moment and the particle size, one can assume that the measured saturation magnetic moment is proportional to the masses of the magnetite and iron samples.[12]

The method described above allow one to determine the concentrations of magnetic phases at any point of the thermomagnetic curve. The characteristic points of the spectrum include T_{max} and T_{min} (see points B and C, respectively, in Fig. 8). The total magnetizations of the samples at these points $J(T_{min})$ and $J(T_{max})$ were measured after heating of the samples to the corresponding temperatures and subsequent cooling to room temperature. The magnetization is due to the formation of Fe_3O_4 and Fe at T_{min} and T_{max}, which was confirmed by XRD. In addition, wüstite FeO was detected at the point C corresponding to the minimum magnetization; this was also confirmed by XRD. Using this procedure for the determination of m at any point of the TM–TPR spectrum, the contents of Fe_3O_4 and Fe at T_{max} and T_{min} were calculated. It was found that the magnetite concentration at the spectral points specified (see above) is independent of the heating rate, being equal to 85% at a hydrogen flow rate of $v_{H_2} = 60$ ml min^{-1}. However, at high heating rates, the magnetite concentration strongly depends on the hydrogen flow rate. At $v_{H_2} < 40$ ml min^{-1}, the magnetite concentration abruptly decreases due to the formation of FeO.

On going to isothermal heating at a specified point of the thermomagnetic curve, one can study the kinetics of particular stages of the reduction $Fe_2O_3 \rightarrow Fe_3O_4 \rightarrow FeO \rightarrow Fe$ (see Fig. 8).[77] Note that traditional methods of investigation cannot distinguish between particular stages of the process. Using the dependence of the temperature of the onset of phase formation on the heating rate, one can study the kinetics of isothermal reduction of the phases listed above at different temperatures. This in turn makes it possible to determine the apparent activation energies of the

corresponding processes. The kinetic curves obtained at different temperatures were checked for the homogeneous reaction space using the affinities of the kinetic curves obtained at different temperatures as the corresponding criteria.

It was found that the kinetics of transition $Fe_2O_3/SiO_2 \rightarrow Fe_3O_4/SiO_2$ in the temperature range from 573 to 615 K is correctly described by the Avrami – Erofeev equation

$$[-\ln(1-\alpha)]^{1/2} = kt, \tag{28}$$

where α is the conversion and k is the rate constant.

Isothermal reduction of Fe_3O_4/SiO_2 to FeO/SiO_2 is characterized by the maximum initial rate and can be described by the model of contracting sphere with diffusion (Yander equation)

$$[1-(1-\alpha)^{1/3}]^2 = kt. \tag{29}$$

The kinetics of isothermal reduction $FeO/SiO_2 \rightarrow Fe/SiO_2$ is also correctly described within the framework of the model of contracting sphere with diffusion.

The TPR spectrum of the catalyst Fe_2O_3/SiO_2 is shown in Fig. 9 and presents the changes in the magnetization and in the rate of hydrogen uptake. Interpretation of TPR spectra of Fe-supported catalysts is often ambiguous owing to the multistaginess of the reduction process and to the interactions of iron oxides with the support resulting, in the case of SiO_2, in the formation of silicates.[72] In some cases, combining TPR with continuous magnetization measurements considerably simplifies the assignment of peaks in the TPR spectrum. The first peak in the TPR spectrum corresponds to the transition $Fe_2O_3 \rightarrow Fe_3O_4$ accompanied by an increase in the magnetization [magnetite (Fe_3O_4) is a ferrimagnet]. Then, the minimum magnetization value is observed at 540 °C as well as the corresponding maximum of the rate of H_2 uptake during the formation of FeO. Subsequent increase in the magnetization and in the rate of hydrogen uptake is related to the formation of metallic iron.

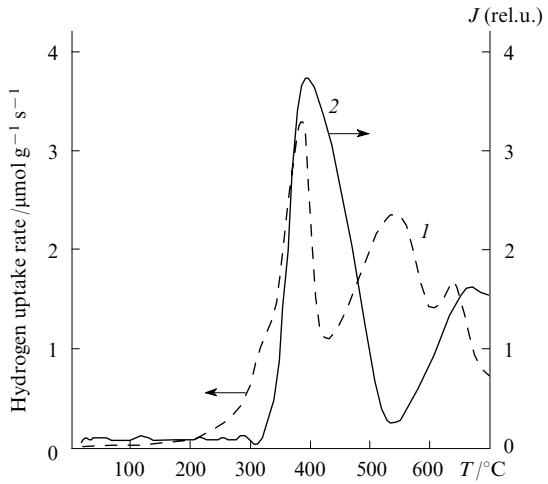


Figure 9. TPR spectrum (*1*) and the temperature dependence of magnetization (*2*) of the catalyst Fe_2O_3/SiO_2.

Continuous magnetization measurements appeared to be a convenient method of investigation of the effect of reduction promoters, such as platinum or copper, on the dynamics of the process.[78] Consider the influence of promoters taking the systems $Pt-Fe/SiO_2$ and $Cu-Fe/SiO_2$ (Figs 10 and 11, respectively) as examples. Hydrogen spillover from platinum to the support and iron oxide is illustrated in Fig. 10. Owing to spillover, the temperature

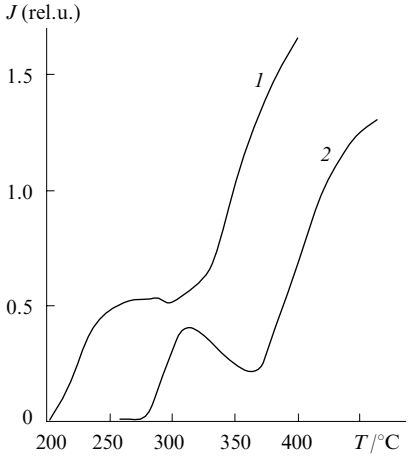


Figure 10. TPR spectra of systems $Pt/Fe/SiO_2$ (*1*) and Fe/SiO_2 (*2*).

of the onset of reduction significantly decreases. It should be noted that the degree of iron reduction in the system $Pt-Fe_2O_3/SiO_2$ is much higher than in the catalyst Fe_2O_3/SiO_2 reduced under identical conditions. Since the average size of Fe-containing particles is proportional to the ratio of the mass of iron to its specific surface area, one should expect an increase in the average particle size for the reduction in the presence of platinum. Indeed, both magnetic measurements and X-ray based characterization of the size of Fe-containing particles showed that the average

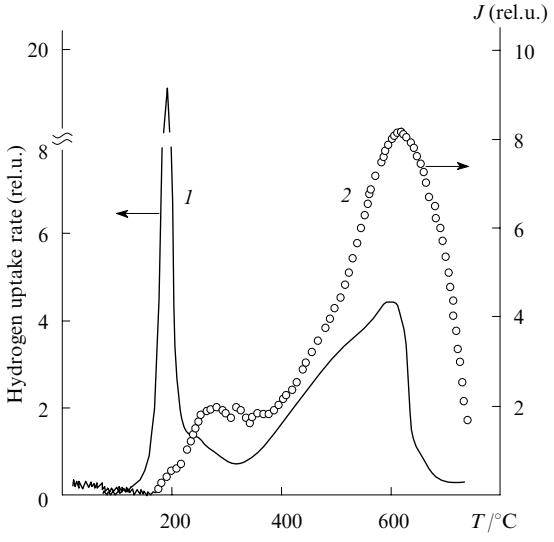


Figure 11. TPR spectrum (*1*) and the temperature dependence of magnetization (*2*) for the system $Cu-Fe/SiO_2$.
Hydrogen uptake rate (rel.u.)

particle size of the catalyst $Pt-Fe_2O_3/SiO_2$ is nearly 20 nm. Thus, the average particle size appreciably increases compared to that of the particles of the catalyst Fe/SiO_2 (15 nm).

The temperature dependences of the magnetization during the reduction of the catalysts Fe_2O_3/SiO_2 and $Pt-Fe_2O_3/SiO_2$ in hydrogen stream show that the use of platinum also causes the temperature of the onset of iron to decrease.

The promoting effect of copper is observed in the TPR spectrum of the system $Cu-Fe/SiO_2$ (see Fig. 11). Here, the first hydrogen absorption peak corresponds to CuO reduction to the metal; the magnetization increases almost simultaneously, thus indicating the formation of magnetite in the system. Clearly, in this case the promoting effect cannot be attributed to hydrogen spillover because hydrogen is adsorbed on copper without dissociation. Nevertheless, continuous magnetization measurements confirm the promoting effect. Promotion by copper (unlike promotion by platinum) leads to a considerable increase in the specific surface area due to the decrease in the average size of iron particles to 12–13 nm. From X-ray based data it follows that the presence of copper in the catalysts $Cu-Fe/SiO_2$ causes the development of microdistortions of the crystal lattice of iron particles.

By measuring the magnetization during TPR one can obtain unique information on the influence of the porous structure of the surface on the dynamics of reduction. Figure 12 presents the TPR spectrum and the changes in the magnetization during the TPR of the catalyst 15% Fe/SiO_2 on S-80 silica gel (large-pore silica gel). The spectrum exhibits two peaks at 280 and 310 °C in the stage of hematite reduction to magnetite. Both peaks correspond to the formation of magnetite, as follows from the temperature dependence of the magnetization. Both peaks in the TPR spectrum are accompanied by an increase in the magnetization and separated by a weak shoulder in the magnetization curve at 300 °C. The magnetite → wüstite transition corresponds to a peak at $T_m = 440$ °C in the TPR spectrum and the minimum value of the magnetization. The mismatch between the peaks in the TPR spectrum and the extrema in the magnetization curve can be explained by the fact that the TPR curve is differential (it characterizes the rate of the process), whereas the magnetization curve is an integral characteristic. Therefore, the peak in the TPR spectrum corresponds to an extremum in the first derivative of the magnetization curve.

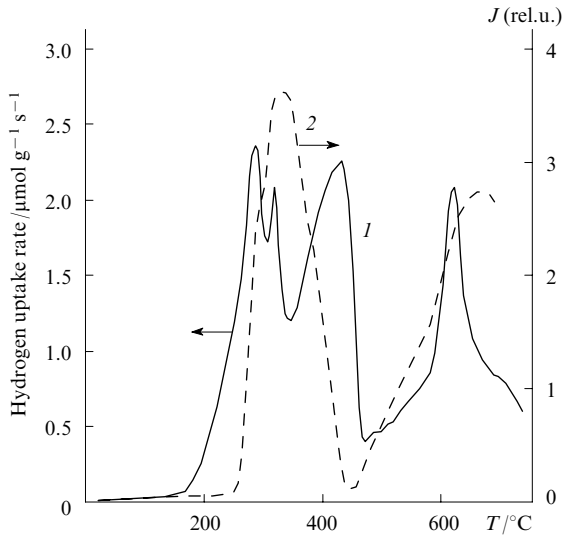


Figure 12. TPR spectrum (*1*) and the temperature dependence of magnetization (*2*) during TPR of the catalyst 15% Fe/SiO_2 on C-80 silica gel.

The wüstite → iron transition also proceeds in two steps, as confirmed by a noticeable change in the slope of the magnetization curve at 570 °C.

Figure 13 illustrates an approximation of the TPR spectrum considered above by Gaussian curves. An analysis of the results obtained taking into account the changes in the magnetization during the reduction suggests that:

— the first peak at 250 °C is not related to the change in the magnetization and is probably due to the desorption of water from silica gel;

— the peaks 1-1, 1-2 and 1-3 correspond to the processes $Fe_2O_3 \rightarrow Fe_3O_4$, $Fe_3O_4 \rightarrow FeO$ and $FeO \rightarrow Fe$, respectively; this sequence of transformations also corresponds to the peaks 2-1, 2-2 and 2-3, respectively.

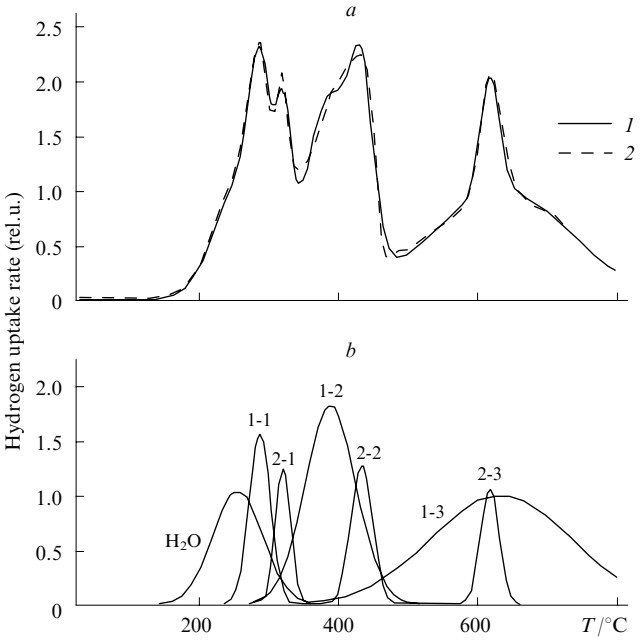


Figure 13. Results of approximation of the TPR spectrum shown in Fig. 12 by Gaussian peaks (*a*) and deconvolution of experimental data (*b*).
Experimental TPR spectrum (*1*) and approximation (*2*).

Thus, the TPR spectrum in question characterizes two concurrent processes shifted relative to each other on the temperature scale. The shift is due to the fact that the S-80 silica gel has a relatively small specific surface area ($80\ m^2\ g^{-1}$) and in the preparation of a concentrated catalyst, some proportion of iron oxide is present in the form of large hematite particles on the outer surface of the support granules. The remaining hematite is distributed within the support pores. Large hematite particles on the surface of silica gel granules are reduced first of all, while smaller hematite particles located in pores are reduced somewhat later (as the necessary temperature is attained).

When using silica gel with a smaller pore diameter, *e.g.*, KSK-2, the order of the reduction stages changes as follows:

$$Fe_2O_3 \longrightarrow Fe_3O_4,$$

$$Fe_3O_4 \longrightarrow FeO,$$

$$FeO \longrightarrow Fe,$$

because KSK-2 has a rather large specific surface area, and iron nitrate is uniformly distributed across the entire surface in the course of impregnation.

Reduction of iron oxides supported on γ-Al_2O_3 shows a much more complicated pattern.[79,80] This is due to strong oxide–oxide interaction in this system,[81] which is accompanied by the formation of numerous iron aluminates with variable stoichiometry. In this case, additional information can be obtained by continuous magnetization measurements because many iron aluminates are magnetic and can be identified based on their Curie temperatures.

A magnetometric study of the reduction of supported oxides under isothermal conditions allows one to obtain the kinetic parameters of reduction in individual stages of the process.[4] It should be noted that traditional methods of investigation of the kinetics of reduction, such as gravimetry or analysis of the composition of exhaust gases, can hardly be used to distinguish between particular stages of the process.

Figure 14 presents the dependences of conversion on the reduced time for the reduction of $Fe_2O_3/SiO_2-Fe_3O_4/SiO_2$, $Fe_3O_4/SiO_2-FeO/SiO_2$ and $FeO/SiO_2-Fe/SiO_2$. Intermediates of the reduction of Fe_3O_4/SiO_2 and FeO/SiO_2 were obtained in the TPR regime. The reduction was terminated upon the attainment of a specified magnetization of the system by replacing hydrogen by inert gas stream and going to isothermal heating. By varying the heating rate in the TPR regime one can change the temperature of formation of the corresponding intermediate.

Isothermal reduction of the starting X-ray amorphous catalyst to Fe_3O_4/SiO_2 (see Fig. 14*a*) showed that in the temperature range from 573 to 615 K the conversion-*vs.*-time plot has sigmoidal shape and is reasonably described by the Avrami–Erofeev equation (28).

The kinetics of isothermal reduction of Fe_3O_4/SiO_2 to FeO/SiO_2, which was obtained analogously, is characterized by the maximum initial rate (see Fig. 14*b*). The process $FeO/SiO_2 \rightarrow Fe/SiO_2$ is also characterized by the dependence of conversion on time, which corresponds to the maximum initial reaction rate (see Fig. 14*c*). Using the data on isothermal reduction, one can show with ease that the processes $Fe_3O_4/SiO_2 \rightarrow FeO/SiO_2$ and $FeO/SiO_2 \rightarrow Fe/SiO_2$ are well described by the model of contracting sphere with diffusion, *i.e.*, the Yander equation (29).

Reduction in the systems Fe_2O_3/Al_2O_3 and Fe_2O_3/ZrO_2 proceeds analogously. For all systems under study one can estimate, more or less accurately, the apparent activation energies of the reduction (E^*) of supported iron oxides.[72]

As the iron concentration increases, the parameter E^* of the process $Fe_2O_3 \rightarrow Fe_3O_4$ regularly increases, whereas the parameter E^* of the process $Fe_3O_4 \rightarrow FeO$ decreases. If hematite particles are rather large, the parameter $E^*(Fe_2O_3 \rightarrow Fe_3O_4)$ only slightly depends on the nature of the support. At the same time, a decrease in the hematite particle size leads to a noticeable decrease in $E^*(Fe_2O_3 \rightarrow Fe_3O_4)$ and to an increase in $E^*(Fe_3O_4 \rightarrow FeO)$.

Interest in the kinetics and mechanisms of reduction of iron oxides is first of all due to the use of iron catalysts in various processes, in particular, the Fischer–Tropsch synthesis. In some cases, magnetic methods of investigation of catalysts allow one to establish correlations between the particle size of the supported metal and the selectivity. Measurements of the blockage temperature (see Section III) of Fe-containing mesoporous molecular sieves[82] (MSM-41) with different iron concentration showed that the iron-

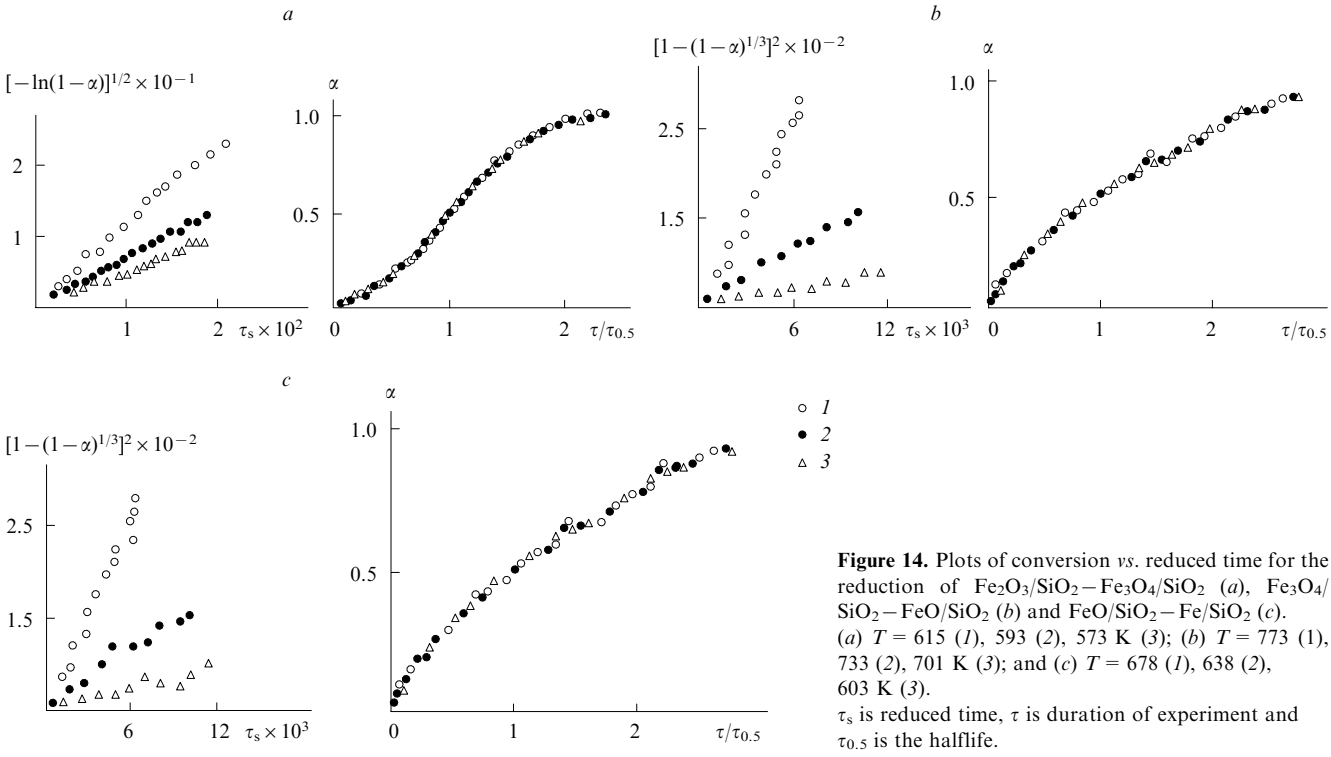


Figure 14. Plots of conversion *vs.* reduced time for the reduction of $Fe_2O_3/SiO_2-Fe_3O_4/SiO_2$ (*a*), $Fe_3O_4/SiO_2-FeO/SiO_2$ (*b*) and $FeO/SiO_2-Fe/SiO_2$ (*c*). (*a*) T = 615 (*1*), 593 (*2*), 573 K (*3*); (*b*) T = 773 (1), 733 (*2*), 701 K (*3*); and (*c*) T = 678 (*1*), 638 (*2*), 603 K (*3*).
τ_s is reduced time, τ is duration of experiment and $\tau_{0.5}$ is the halflife.

depleted catalyst contains superparamagnetic iron particles located in pores of the support. Contrary to this, the iron-rich catalyst contains large particles arranged on the outer surface of zeolite granules. The highest selectivity in the reaction of cyclohexene oxidation was found for the catalyst containing superparamagnetic iron particles. Among the catalysts of the Fischer–Tropsch synthesis, the highest selectivity with respect to C^{5+} (see †) was obtained for at least 10-nm iron particles.[83]

2. The kinetics of iron carburization in the course of CO hydrogenation

The kinetics of iron carburization is of interest because it accompanies the CO hydrogenation on iron catalysts. Three types of active carbon are formed on the surface of Fe/Al_2O_3.[84] The following carbides are described in the literature: FeC, hexagonal ε-Fe_2C ($T_C = 653 \pm 10$ K), pseudohexagonal ε′-$Fe_{2.2}C$ ($T_C = 723 \pm 10$ K), monoclinic Hegg carbide χ-Fe_5C_2 ($T_C = 478-529$ K according to different sources) and orthorhombic cementite θ-Fe_3C ($T_C = 481 \pm 3$ K).[85–88] Each of them is involved in the Fischer–Tropsch synthesis on iron catalysts.[89] The composition of carbides depends on the H_2 : CO ratio, the iron particle size, degree of iron reduction and temperature. The first 10 s of the reaction are characterized by the appearance of highly reactive particles CH_x. Then, less reactive particles CH_y are formed and undergo transformation to surface carbide as the reaction medium is replaced by inert gas. The low-reactive species whose concentration increases rather slowly have little effect on the reaction rate. In addition, inert graphite-like carbon favouring a decrease in the catalyst activity is deposited on the catalyst surface during the reaction. Unique properties of iron (high reactivity in the Fischer–Tropsch synthesis and ready formation of metal carbides) are responsible for many difficulties in the elucidation of the mechanism of the Fischer–Tropsch synthesis.

Carburization of iron in molten catalysts during CO hydrogenation has been studied in detail.[90] The process is well described within the framework of the diffusion kinetics. But since we are first of all interested in topochemical processes involving nanoparticles, the emphasis will be placed on the Fe-supported catalysts of the Fischer–Tropsch synthesis whose mechanism is well documented.[91]

Almost all difficulties in the establishment of the mechanism of CO hydrogenation are due to the fact that we don't know what happens with CO during and immediately after its adsorption, what particles are formed involving the carbon atom, how oxygen binds and how iron behaves. Under the synthesis conditions, one deals with dissociative (85%) and associative (15%) adsorption of CO, carbon being bound to two iron atoms.[92] After adsorption of reactants, two processes begin, namely, the interaction of carbon with iron (carburization) and with hydrogen (Fischer–Tropsch synthesis), but interrelations between them still remain unknown.

There is a considerable body of data on the compositions of the carbides formed; however, the kinetics of carburization has almost not been studied so far. It was assumed that the carburization kinetics is described by a first-order equation,[93] but no quantitative data on the subject are available. The influence of promoters on carburization kinetics was also not studied; nevertheless, it is assumed that, similarly to copper, potassium has no effect on carburization.[94] Interrelations between carburization and synthesis of hydrocarbons are also unknown.

Among the methods most often used in the studies of carburization kinetics, mention may be made of Mössbauer spectroscopy. However, the accuracy of kinetic data is still low. The use of XRD is precluded because of small structural distinctions between iron carbides and small particle sizes.

Surprisingly, studies on the carburization kinetics using continuous *in situ* magnetization measurements appeared to be highly informative and made it possible to answer many questions (see above). Since the specific magnetization of carbides is much lower than that of iron, *in situ* magnetization measurements during CO hydrogenation allow the kinetics to be studied with high accuracy unattainable when using other methods.

Since carburization of iron is a step in CO hydrogenation, it is appropriate to briefly outline peculiar features of the mechanism of the Fischer–Tropsch synthesis. A specific feature of carburization in the Fischer–Tropsch synthesis consists in that it involves hydrogen.

According to Matsumoto and Bennett,[95] carburization of iron in $CO + H_2$ mixture proceeds faster than in CO + Ar mixture. The following reaction was proposed:

$$4\,CO + 6\,Fe + 2\,H_2 \longrightarrow 2\,H_2O + CO_2 + 3\,Fe_2C.$$

ε′-Carbide is usually present in the Fischer–Tropsch synthesis on Fe catalysts promoted by K_2O, Cu and Si.[87] It is thermally unstable in the presence of promoters and can be readily transformed to the Hegg carbide χ-Fe_5C_2 at $T \geqslant 623$ K. Carburization is accompanied by the formation of ε′-carbide and Hegg carbide; only χ-carbide is found in the final stage of the process.[88]

The Fischer–Tropsch synthesis usually results in thermally stable cementite and a readily decomposable Hegg carbide. The stability of iron carbides increases as follows:[87]

$$\varepsilon'\text{-}Fe_{2.2}C < \varepsilon\text{-}Fe_2C < \chi\text{-}Fe_5C_2 < \theta\text{-}Fe_3C.$$

Carbides undergo conversion from one form to another as temperature increases. At 388 K, two carbides (ε and ε′) are formed; only the ε-carbide was detected at 423–458 K; at 493–673 K, it is converted to the Hegg carbide and then cementite is formed at 723 K.[96]

It should be noted that identification of the carbides ε′-$Fe_{2.2}C$ and ε-Fe_2C by XRD is ambiguous.[97] Opinions are different whether the ε′- or ε-carbide is an insertion phase.[88] The lattice constants of the ε′- and ε-iron carbides determined by different researchers are significantly different; this may lead to incorrect identification of carbides based on XRD data. In this case, additional information on the compositions of the carbide phases (Curie temperatures of the carbides formed are different) can be obtained from magnetic measurements.

Carburization is also of interest as a model reaction for investigations of heterogeneous processes in the gas–solid system. Taking this reaction as an example, one can study, in particular, the effect of the particle size on the specific rate of the heterogeneous process. It is important that the mechanism of carburization considered as a step of a more complex process of CO hydrogenation is significantly different from that of the carburization of iron by pure carbon

† C^{5+} denotes hydrocarbons with the backbone 5 and more carbon atoms long.

monoxide. In the latter case, the process is much slower and results in another phase composition of products.

Based on the results of magnetization measurements before and after carburization and knowing the specific magnetization of each phase, one can determine the number of corresponding carbides. This is possible because the contents of carbides are related to the mass of iron in the sample before carburization by stoichiometric relations. Quantitative determination of ε'- and χ-carbides is reduced to solution of the system of two linear equations with two unknowns

$$X_1 M(\varepsilon') j(\varepsilon') + X_2 M(\chi) j(\chi) - J_C = 0, \tag{30}$$

$$j(\mathrm{Fe})\{(M(\varepsilon') - 12)X_1 + (M(\chi) - 12)X_2 - J_{\mathrm{Fe}} = 0,$$

where X_1 and X_2 are the numbers of moles of the ε'- and χ-carbides, respectively; $M(\varepsilon')$ and $M(\chi)$ are the molecular masses of the carbides ε'- and χ-$Fe_{2.5}C$, respectively; $j(i)$ is the specific magnetization of the ith phase at room temperature; and J_C and J_{Fe} are the measured magnetizations of carbon and iron, respectively.

During carburization the total magnetization of the sample under study decreases because for any temperatures one has $j(\mathrm{Fe}) > \sum j(i)$. This allows one to calculate the degree of carburization of iron as follows:

$$\alpha(t) = \frac{J_0^{(T)} - J_c^{(T)}(t)}{J_0^{(T)} - J_c^{(T)}(\infty)}, \tag{31}$$

where $\alpha(t)$ is the degree of carburization at the instant t, J_i is the magnetization of the sample at temperature T (the subscript i denotes: $i = 0$ for the initial sample; $i = c$ during carburization) at the instant t and after completion of carburization $J_c^{(T)}(\infty)$. Continuous magnetization measurements during CO hydrogenation allow the reaction kinetics to be studied.

It should be noted that making use of this method of investigation of carburization kinetics imposes some restrictions on the phase compositions of the systems under study. For instance, calculations using expression (31) are incorrect if the system contains magnetite which in this case also contributes to the total magnetization. The specific rate of carburization was determined from the relation

$$w = \frac{n}{s}\frac{\mathrm{d}\alpha}{\mathrm{d}t}, \tag{32}$$

where n is the number of moles of iron, s is the specific surface area of iron and α is the degree of carburization.

The classical phenomenological theory of the kinetics of gas–solid reactions considers the situation after nucleation of the solid product, where heterogeneous inclusions appear within the solid. At very low degrees of conversion, the reaction proceeds in the homogeneous region. This is the so-called pre-nucleus period which determines the regularities of nucleation and, thus, the course of the subsequent process.[56] It was found that at low degrees of carburization ($\alpha < 0.03$), the temporal dependence of the carburization rate has a characteristic minimum. An abrupt initial decrease in the rate of carburization is due to the fact that nucleation of the solid product reqiures the overcoming of some strength. This effect is most pronounced at carburization temperatures below 523 K. The number of nuclei of the carbide phase is time dependent[98,99]

$$N = z_0 S[1 - \exp(-k_2 t)], \tag{33}$$

where z_0 is the number of potential nucleation sites, S is the surface area, and k_2 is the rate constant for nucleation. The dependence of the degree of carburization on time is well described by the Avrami–Erofeev equation

$$\alpha(t) = 1 - \exp\left\{-k_1'\left(t - \frac{1}{k_2}\left[1 - \exp(-k_2 t)\right]\right)\right\}, \tag{34}$$

where

$$k_1' = k_1 z_0 \frac{S}{n},$$

k_1 is the rate constant for nucleation of the carbide phase.

Processing of experimental data in the coordinates of Eqn (33) makes it possible to determine the rate constants k_1 and k_2 by the least squares method using conventional software.

Clearly, the method of continuous magnetization measurements can also be used in studies of other topochemical processes accompanied by changes in the magnetization of the system under investigation. Of course, the temperature at which the experiments are performed should be higher than the Curie temperature of the magnetic subsystem.

The dependences of the degree of conversion on the reduced time for the catalyst Fe/Al_2O_3 at 493, 523 and 550 K are shown in Fig. 15.

The observed carburization kinetics can be described using at least two alternative models. One of them assumes that the limiting stage is a reaction in the adsorbed layer. In the other model, the carburization reaction is considered as a topochemical process with the formation of the carbide phase as the slow step. In the former case, k_2 is treated as the rate constant for a process localized within the adsorbed layer; in the latter case, k_2 is the parameter of a process occurring in the near-surface layer and characterizes the nucleation rate of the carbide phase.

To answer the question which of the two models is more realistic, we carried out an experiment using the 'response' technique. At a specified degree of carburization, the mixture $CO + H_2$ was replaced by H_2, the catalyst

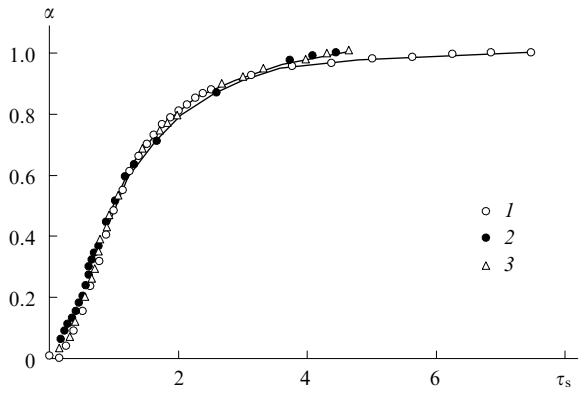


Figure 15. Conversion plotted *vs.* reduced time for the catalyst Fe/Al_2O_3 at 493 (*1*), 523 (*2*) and 550 K (*3*).

15% Fe/SiO_2 was exposed to H_2 stream to reach a steady-state degree of carburization and then hydrogen was again replaced by the mixture $CO + H_2$. This experiment gave the temporal dependence of the carburization rate shown in Fig. 16. As can be seen, the carburization rate passes through a maximum only when hydrogen is for the first time replaced by the $CO + H_2$ mixture (region *I*). Subsequently, the reaction continues at the maximum initial rate (regions *II* and *III*). If the reaction rate was determined by the processes in the adsorbed layer, the supply of a next portion of the $CO + H_2$ mixture would cause the formation of the adsorbed layer from the very beginning and the reaction rate would every time pass through a maximum. However, this is not the case and, therefore, the formation of the adsorbed layer takes a much shorter time compared with the relaxation time of the carburization rate. This is an argument in favour of the nucleation model.

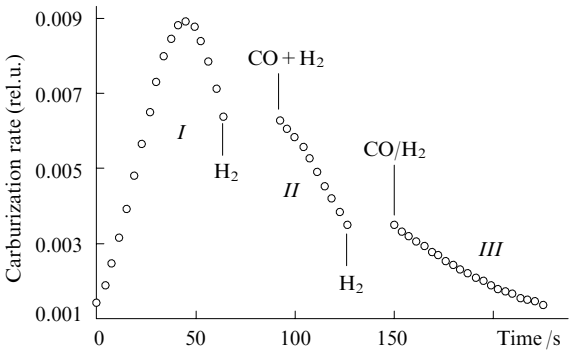


Figure 16. Carburization rate plotted *vs.* time (results of experiment using the 'response' technique).

We also studied the influence of promoters (potassium and copper) on the kinetics of carburization.[100] The rate of carburization is plotted *vs.* time for the catalysts Fe/SiO_2 and $Fe-K/SiO_2$ in Fig. 17. As can be seen, the rate of carburization remains almost unchanged, but the time needed to attain the maximum reaction rate considerably increases. Subsequent analysis showed that the nucleation rate characterized by the constant k_2 substantially decreases while the effective activation energy of nucleation appreciably increases in the presence of a promoter.

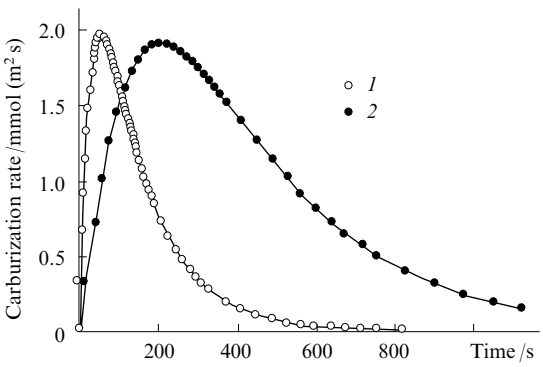


Figure 17. Carburization rates plotted *vs.* time for the catalysts Fe/SiO_2 (*1*) and $Fe-K/SiO_2$ (*2*).

Contrary to promotion by potassium, promotion of supported Fe catalysts by copper leads to a great acceleration of carburization. Depending on the procedure for the addition of promoter, the nucleation rate decreases compared to the unpromoted Fe-containing catalyst if copper is present in the form of individual particles and increases if a solid solution of copper in iron is formed.

In the presence of platinum, the rate constant for nucleation of the carbide phase is more than doubled compared to the unpromoted catalyst ($k_2 = 0.015$ for Fe/Al_2O_3 and 0.04 for $Pt-Fe/Al_2O_3$). It should be noted that no platinum–iron alloys are formed in this case, as indicated by the study of the thermomagnetic curves of the platinum-containing catalysts.

Thus, using magnetization measurements during the catalytic reaction, we for the first time studied the kinetics of iron carburization on the support in the course of CO hydrogenation.

VIII. Topochemical processes on Co-containing catalysts

Cobalt catalysts are optimal for the synthesis of long-chain hydrocarbons in the Fischer–Tropsch process. They are stable and the processes involving them are characterized by high degrees of conversion and high yields of hydrocarbons. The Fischer–Tropsch reaction proceeds on metallic cobalt particles supported on Al_2O_3, SiO_2, TiO_2, *etc.* Unlike its oxides, metallic cobalt exhibits ferromagnetic properties. Therefore, interpretation of the data is simpler than in the case of iron catalysts. The oxides Co_3O_4 and CoO show antiferromagnetic properties at low temperatures. At the Néel temperature [30 K for Co_3O_4 (Ref. 101) and 288 K for CoO (Ref. 102)], they undergo antiferromagnetic and paramagnetic transformations. At room temperature and at elevated temperatures, Co_3O_4 and CoO exhibit paramagnetism. This is the reason why the magnetization of the oxidized cobalt catalyst in magnetic field is very low. We believe that the contribution of cobalt oxides to the total magnetization is at most 5%. Therefore, the magnetometric method applied to Co-containing catalysts shows a very high sensitivity towards metallic cobalt.

Magnetic measurements for cobalt catalysts are carried out both *in situ* and *ex situ*. The former kind of experiments involves the magnetization measurements in the course of pre-treatment of the catalyst and during the catalytic reaction. The Curie temperature of cobalt is rather high ($\sim$1400 K); therefore, most reactions on cobalt can be studied *in situ*. By combining traditional methods of investigation of catalysts (TPR and continuous magnetization measurements) one can obtain comprehensive information on the catalyst. *Ex situ* experiments allow one to determine the parameters of catalysts that should be kept in the reaction medium prior to being placed into the magnetometer. In any case, this can be done without exposure of the catalyst to air.

Based on the results of magnetic measurements for the Co-containing catalysts for the Fischer–Tropsch synthesis, one can determine the degree of reduction (concentration of metallic cobalt can be measured *in situ* at any instant), obtain information on the oxidation kinetics of cobalt particles and calculate their size.

1. Reduction of cobalt catalysts

As mentioned above, reduction of supported cobalt oxides can be studied using continuous magnetization measurements. In this case, the method is somewhat less informative than when applied to the Fe/support systems, because only metallic cobalt possesses the magnetic properties; however, interpretation of experimental data is simplified. The formation of metallic cobalt particles can be detected at relatively low concentrations as in, *e.g.*, the case of $La(Co, Fe)O_3$ and perovskites.[103, 104] Since the Curie temperature of cobalt is high, one can investigate processes occurring at relatively high temperatures. A combination of TPR, a traditional method of investigation of catalysts, with simultaneous continuous magnetization measurements appeared to be fruitful.

Unlike traditional TPR carried out in dilute hydrogen, magnetic measurements can be carried out in pure hydrogen; the data on the degree of reduction of cobalt obtained in this case are more reliable. The use of an $Ar + 5\%$ H_2 mixture in TPR experiments leads to lower degrees of reduction of cobalt than in pure hydrogen.[16] The magnetometric method allows one to determine the temperature corresponding to the onset of formation of metallic cobalt, which is important for the description and prediction of the catalytic properties of cobalt catalysts for the Fischer–Tropsch synthesis.

At least three oxides (Co_2O_3, Co_3O_4 and CoO) can form during the preparation of Co- and Fe-supported catalysts. At high temperatures, CoO interacts with such oxides, as Al_2O_3 (Ref. 105) and SiO_2,[106] to give $CoAl_2O_4$ and Co_2SiO_4, respectively. The mechanisms of these reactions usually occurring in oxide mixtures at temperatures above 1200 K have been rather well studied. For instance, the mechanism of counter-diffusion of Co^{2+} and Al^{3+} ions[107] dominates in the formation of $CoAl_2O_4$, whereas Co_2SiO_4 is thought to be formed through counter-diffusion of Co^{2+} ions and holes through a layer of the product and simultaneous transfer of oxygen through the gas phase.

Probably, owing to small size of cobalt oxide particles, such processes in supported systems may also proceed at lower temperatures, *viz.*, the catalyst preparation temperatures.

Processes occurring during the reduction of the system Co_3O_4/SiO_2 were studied using a microporous silica gel KSS-3 (specific surface area (s) 450–600 $m^2\ g^{-1}$, average pore diameter (d) 5.6–8 nm) and two macroporous silica gels, KSK-2 ($s = 350\ m^2\ g^{-1}$, $d = 15$ nm) and S-80 ($s = 80\ m^2\ g^{-1}$, $d = 50$ nm). Catalysts were prepared by impregnation with cobalt nitrate (10 mass % Co) followed by calcination at 300 °C up to complete decomposition of the nitrates. The catalysts were studied by TPR and continuous magnetization measurements. In the system Co–Si–O, only metallic cobalt has a nonzero magnetization; therefore, the magnetization measurements in the course of TPR give unique information on the dynamics of the reduction process. Figure 18 presents the temperature dependences of the rate of the changes in the magnetization dJ/dT in the course of TPR for the catalysts Co_3O_4/SiO_2 prepared on silica gels with different porosity.

In all TPR spectra shown, the rate of the change in the magnetization dJ/dT is approximately equal to the rate of hydrogen uptake. Thus, in the temperature range 250–750 °C, the TPR spectrum corresponds to the reduction of CoO to Co. Non-monotonic changes in the reduction rate result from the effect of the porous structure.

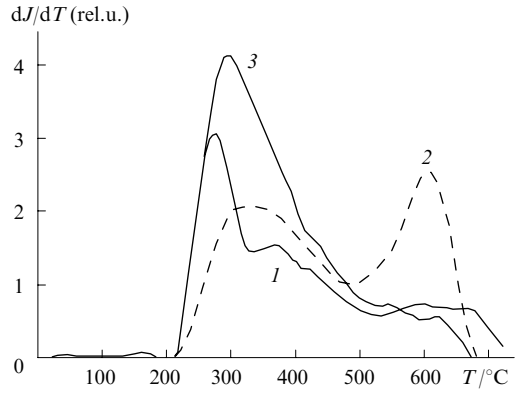


Figure 18. Temperature dependences of the rate of the change in the magnetization during TPR of Co_3O_4/SiO_2 catalysts prepared on silica gels with pore sizes of 7 (*1*), 15 (2) and 50 nm (*3*).

Three temperature intervals can be distinguished for the reduction of CoO to Co, *viz.*, 200–350, 350–500 and 500–750 °C. Each of them corresponds to a particular peak in the temperature dependence dJ/dT. Based on the data shown in Fig. 18, one can approximately calculate the relative amount of cobalt formed in the reduction in each temperature interval.

The first temperature interval corresponds to reduction of the largest particles located in pore throats and on the outer surface of silica gel granules. As the pore size in the support decreases, the total degree of reduction of cobalt also decreases due to encapsulation of CoO particles in narrow silica gel pores. Also, in narrow pores, exchange of protons of the surface silanol groups for Co^{2+} ions during the impregnation of the support is possible because the pH value can increase from 2 (this corresponds to neutral SiO_2 surface) to 4.4–4.7 depending on the degree of pore filling.[108] Owing to ion exchange in the impregnation stage, subsequent calcination results in silicates. Therefore, a decrease in the degree of reduction with the increase in the specific surface area of the support (decrease of average pore size) is due to not only encapsulation, but also formation of the surface cobalt silicate. A comparison of TPR of the catalysts Co_3O_4/SiO_2 suggests that position of the first peak is not affected by the porous structure of the support surface. In other words, the course of the reaction

$$Co_3O_4 + H_2 \longrightarrow 3\,CoO + H_2O$$

is not affected by mass transfer in pores of the support, whereas the rate of CoO reduction to metal is limited by mass transfer processes. We believe that this situation is determined by the relatively low temperature of the interaction between Co_3O_4 and H_2. Most probably, in this temperature interval the reaction proceeds in the kinetic regime and mass transfer within pores is a rather fast process.

A similar situation was observed for the catalyst 15% $Co/ZrO_2 + 6\%$ Y_2O_3. The TPR spectra of this catalyst calcined prior to reduction at 300 and 600 °C for 30 min are shown in Fig. 19 along with the temperature dependences of magnetization during TPR.[74] As can be seen, the onset of magnetization in the system is preceded by the appearance of a peak in the TPR spectrum, which corresponds to the reduction $Co_3O_4 \rightarrow CoO$. The next peak in the spectrum is

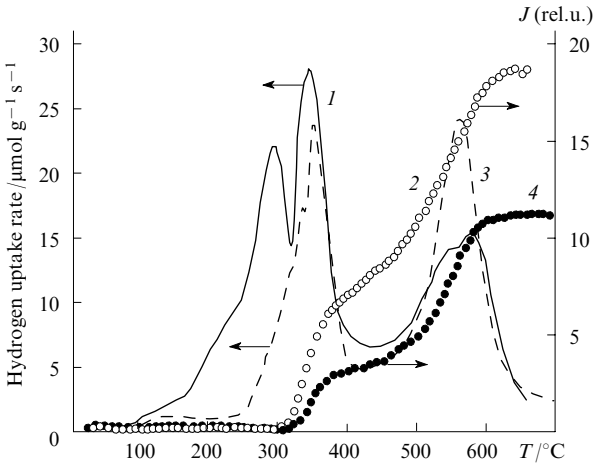


Figure 19. TPR spectra (*1*, *3*) and the temperature dependences of magnetization (*2*, *4*) of the catalyst 15% $Co/ZrO_2 + 6\%$ Y_2O_3 calcined at 300 (*1*, *2*) and 600 °C (*3*, *4*) for 30 min.

followed by an increase in the magnetization and therefore corresponds to the reduction $CoO \rightarrow Co$. As the calcination temperature increases, the area under the first peak decreases. In the TPR spectrum of the sample calcined at 600 °C, this peak disappears. This is probably due to a decrease in the stability of the oxide Co_3O_4 on heating and to the transformation $Co_3O_4 \rightarrow CoO$.

At $T > 500$ °C, the TPR spectrum exhibits the third peak accompanied by an increase in the magnetization and, therefore, corresponding to the appearance of an additional amount of metallic cobalt in the system. This peak is not associated with reduction of a hard-to-reduce Co–Zr oxide. This type of two-step reduction of CoO can be due to diffusion retardation of the reduction in micropores of the support. It is noteworthy that on going to mesoporous supports, reduction proceeds in the same temperature interval. Thus, the use of the magnetometric method makes it possible to extract a much greater amount of information from TPR spectra and to improve its quality.

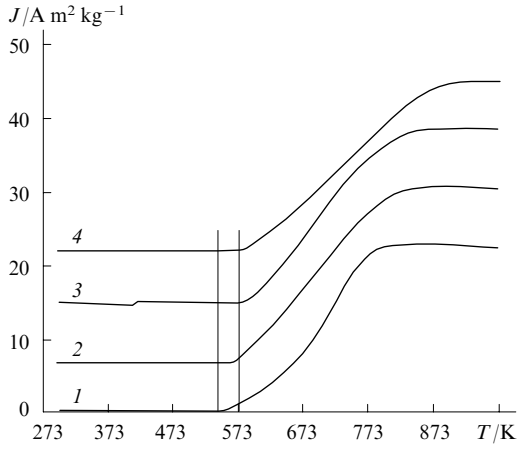


Figure 20. Temperature dependences of magnetization in the course of reduction of the catalyst Co/Al_2O_3 calcined at 473 (*1*), 643 (*2*), 673 (*3*) and 773 (*4*).

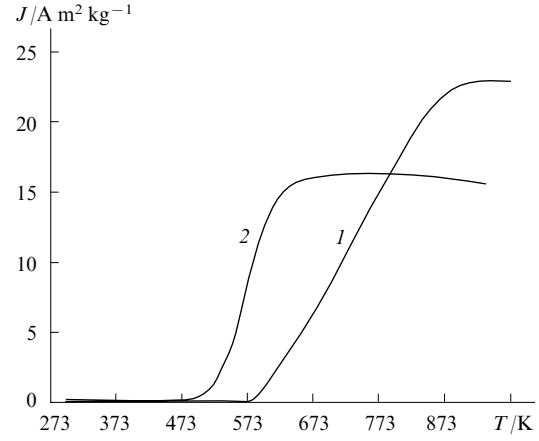


Figure 21. Temperature dependences of magnetization in the course of reduction of cobalt in the catalytic systems Co/Al_2O_3 (*1*) and Co – 0.1 mass % Pt/Al_2O_3 (*2*).

The temperature dependences of magnetization for the systems Co/Al_2O_3 and $Co-Pt/Al_2O_3$ in pure hydrogen are shown in Figs 20 and 21. Clearly, the temperature corresponding to the appearance of metallic cobalt in the catalyst Co/Al_2O_3 depends on the calcination temperature.[109] Cobalt was detected at 547 K in the catalyst calcined at 473 K and at 570–581 K in the catalysts calcined at higher temperatures (643, 673, 773 K). In the system Co/SiO_2, the reduction of cobalt proceeds easier if the catalyst is calcined at moderate temperatures (from 673 to 423 K, see Ref. 110). These effects were explained by differences in the interaction between cobalt and support in the catalysts Co/Al_2O_3 and Co/SiO_2. Promotion by noble metals (Pt, Ru, Re) can also lead to significant changes of the reduction of cobalt.[111] Figure 21 shows that in the system Co – 0.1 mass % Pt/Al_2O_3, cobalt is reduced at 463–473 K (*cf.* $T > 573$ K with no platinum). The magnetometric method can also be used to explain the mechanism of the reduction of cobalt.

The temperature dependences of the reduction rate of cobalt (dJ/dT is the change in the magnetization with temperature) in the system Co – 0.1 mass % Pt/Al_2O_3 at different heating rates in hydrogen are shown in Fig. 22. The differential magnetization is proportional to the rate of formation of metallic cobalt. The position of maximum of the reduction rate depends on the heating rate; the maximum value of the reduction rate is attained at lower temperatures if the catalyst is heated at a lower rate. Therefore, the formation of cobalt is an activated process. The energy of formation of the metal phase can be calculated by the following equation:[112]

$$\frac{d(\ln \Phi/T_m^2)}{d(1/T_m)} = -\frac{E}{R}, \qquad (35)$$

where Φ is the heating rate, T_m is the temperature corresponding to maximum reduction rate and E is the activation energy. In this method, the activation energy is calculated using the slope of the dependence of $\ln \Phi/T_m^2$ on $1/T_m$. The activation energies of formation of cobalt during the reduction of cobalt in the systems Co/Al_2O_3 and Co – 0.1 mass % Pt/Al_2O_3 are 130 and 60 kJ mol^{-1}, respectively.[110] Taking into account these results, in particular, it

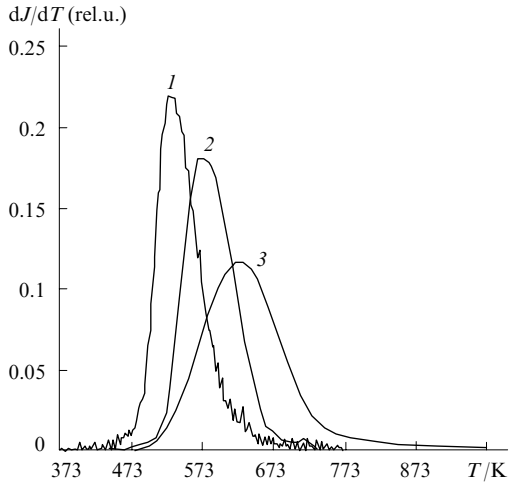


Figure 22. Temperature dependences of the rate of cobalt reduction in the catalyst Co – 0.1 mass % Pt/Al_2O_3 at heating rates of 9 (*1*), 28.2 (*2*) and 102 deg min^{-1} (*3*).

was found that the activation energy of reduction is halved in the presence of 0.1 mass % Pt.

Other promoters of the reduction of cobalt were also studied. Selective synthesis of higher alcohols from the synthesis gas is a particular kind of the Fischer – Tropsch process, which is used in the IFP technology.[113,114] The process uses the catalyst Co/Al_2O_3 prepared by codeposition with promoters (Cu, Zn and Na). A TM – TPR study showed that copper is a better promoter in the reduction of cobalt owing to two effects:

— copper decreases the concentration of cobalt ions localized in the hard-to-reduce spinel Co/Al_2O_3;

— copper obtained by low-temperature reduction of oxide can be used as catalyst for cobalt reduction.[115]

Undoubtedly, *in situ* magnetic measurements under the conditions of the Fischer – Tropsch synthesis are not always possible because high pressure and temperature are needed. However, the so-called 'pseudo *in situ*' method can be used.[116] It should be noted that in the reactor the Co catalyst is covered by a layer of hydrocarbon formed in the Fischer – Tropsch synthesis. It is assumed that the catalyst can undergo re-oxidation when being moved from the reactor to the magnetometer and during the magnetic measurements. Unoxidized Co/Al_2O_3 catalyst under the conditions of the Fischer – Tropsch synthesis was characterized as follows: 503 K, 20 bar ($H_2 + CO$), conversion 50 and 70%, a slurry-reactor (diameter 0.9 m, capacity 13 640 kg day^{-1}). The degree of reduction was calculated from the saturation magnetization; it should not decrease with time. It was reported[1,117,118] that re-oxidation of supported cobalt nanoparticles by water formed in the Fischer – Tropsch process is the main reason for deactivation of the catalyst. However, an analysis of magnetic measurement data suggests[112] that re-oxidation of cobalt particles can be excluded in industrial reactors by thorough control of the pressure of water vapours and hydrogen.

The stability of metallic cobalt under the conditions of the Fischer – Tropsch synthesis (523 K, 50 bar, $2H_2 + CO$, gas mixture flow rate of 104 h^{-1}) is related to the peculiar features of the catalyst.[111] The magnetization of the Co/Al_2O_3 catalyst selective towards hydrocarbons remains unchanged in the course of reaction, whereas the observed deactivation of the catalyst is associated with deposition of carbon (neither bulk oxide nor carbide are formed). Under identical conditions, the Cu(Na, Zn)-promoted Co/Al_2O_3 catalyst selective towards higher hydrocarbons loses metallic cobalt, which is associated with the formation of Co_2C.[108]

2. The kinetics of oxidation of cobalt nanoparticles

Research on the oxidation of small metal particles in supported catalysts is necessary for solving practical and theoretical problems. It is important to know the optimum conditions for passivation of catalysts after their preparation. Also, a metal, which is the active component of the catalyst, is often oxidized during the catalyst operation. This requires elucidation of specific features of the oxidation of small metal particles.

From the theoretical point of view, it is convenient to study the size effects in topochemical reactions taking the oxidation of metal nanoparticles as an example. *In situ* continuous magnetization measurements allow one to carry out effective experimental investigations of processes of low-temperature (from 280 to 500 K) oxidation of small ferromagnetic metal particles in supported catalysts.

During oxidation, the magnetization decreases from the initial value corresponding to the reduced sample (J_0) to the value $J(t)$ at the instant t. Assuming a constant number of metallic cobalt particles, the magnetization J_0 will be proportional to R^3 (R is the average radius of cobalt particles). The thickness of the oxide layer (h) can be determined as follows:

$$h = R\left[1 - \left(\frac{J(t)}{J_0}\right)^{1/3}\right]. \qquad (36)$$

When thick oxide films are formed, the electric field gradient is very small and mass transfer is determined by the concentration gradients only. Under these conditions, oxidation obeys a second-order (parabolic) law, as follows from Wagner's theory.[119] When thin oxide films are formed, especially at low temperatures, when the diffusion of ions is hampered, the electric field gradient begins to play the key role. The kinetics of formation of thin oxide films at low temperatures is quite correctly described by the Cabrera – Mott theory[120] which predicts the existence of a critical temperature below which the film reaches the limiting thickness (a few tens of Ångström) and then its fast growth stops. Below the critical temperature, the relation between the thickness of the oxide film and the temperature is as follows:

$$h = \frac{Veb}{(W - 39k_BT)}, \qquad (37)$$

where V is the electric potential in the oxide layer; e is the electron charge; b is approximately equal to half the interplanar distance in the crystal lattice of the oxide; and W is the work required for the transfer of the cationic vacancy from the surface to the bulk. From expression (37) it follows that the limiting thickness exists only at temperatures lower than $W/39k_B$.

The thickness of the oxide layer is plotted *vs.* time during the isothermal oxidation of cobalt particles in the system 10 mass % Co/Al_2O_3 at different temperatures in Fig. 23. As can be seen, the growth of the oxide film stops as some thickness, which depends on temperature. This pattern of

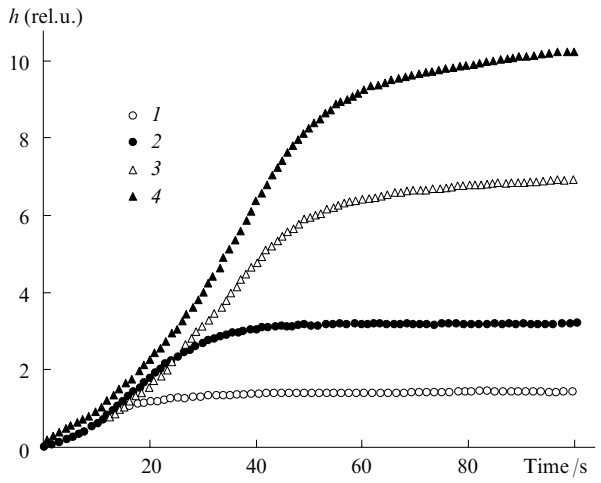


Figure 23. Thickness of the oxide layer plotted *vs.* time for isothermal oxidation of cobalt particles in the system 10 mass % Co/Al_2O_3 at 293 (1), 373 (*2*), 443 (*3*) and 484 K (*4*).

the oxidation reaction qualitatively corresponds to the Cabrera–Mott model.[120] By conducting non-isothermal oxidation one can obtain the TPO spectrum, which characterizes the dependence of the oxidation rate on temperature. The oxidation rate is determined from the rate of the decrease in the magnetization; therefore, in our case the TPO spectra characterize only the decrease in the mass of metallic cobalt. This is different from conventional TPO method in which the rate of oxygen uptake is measured.

The TPO spectrum for the catalyst 10 mass % $Co/ZrO_2 + 6\%\ Y_2O_3$ is shown in Fig. 24.

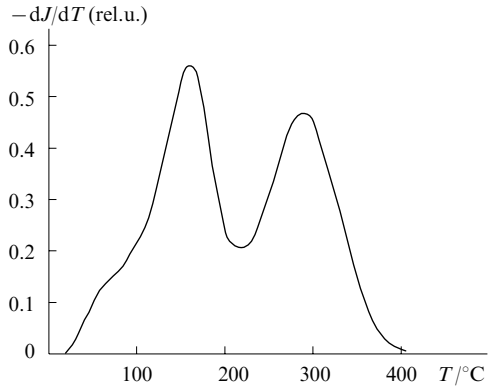


Figure 24. TPO spectrum of the catalyst 10 mass % $Co/ZrO_2 + 6\%\ Y_2O_3$.

To answer the question why the TPO spectrum exhibits more than one maximum, the proportion of superparamagnetic cobalt particles in different stages of oxidation was determined. The larger the proportion of superparamagnetic particles the smaller the average size of cobalt particles in the catalyst. Measurements of the residual magnetization in the systems under study showed that in all cases the proportion of superparamagnetic particles decreased on going from the first to the second peak in the TPO spectrum. It follows that the first TPO peak is due to the oxidation of relatively small cobalt particles, whereas the second peak corresponds to the oxidation of larger metal particles.

Thus, the TPO spectra include information on the size distribution of supported metal particles; however, this information is difficult to extract within the framework of conventional TPO method because the spectrum usually has a rather complex pattern. Combining TPO and *in situ* magnetization measurements allows one to see the determination of particle size distributions for catalysts in a new light. When using a magnetometer as detector, the pattern of the TPO spectrum essentially simplifies. For such metals as nickel and cobalt, one can assess the character of the size distribution of metal particles. Nevertheless, application of this method to supported Fe catalysts faces some difficulties because magnetite formed in the first stage of oxidation also has a nonzero magnetization.

3. Size determination of metallic cobalt particles

Size determination of cobalt particles is based on the relation between the magnetization and the magnetic field strength. In the text below we describe the methods used to determine the size of cobalt particles in the supported Co catalysts. First of all, it should be noted that correct construction of a size distribution for nanoparticles is only possible for an ensemble of non-interacting single-domain particles. For cobalt, these are particles at most 20 nm in size.[17, 23, 49]

To ensure that the system under study contains no particles larger than 20 nm in size, we proposed a method based on partial 'mild' oxidation of cobalt nanoparticles. As mentioned above, at relatively low temperatures the oxidation of cobalt particles proceeds by the Cabrera–Mott mechanism[120] involving the formation of thin oxide films on the surface of metal particles. As a result, the effective particle size decreases. Also, the plot of coercive force *vs.* cobalt particle size has a pattern with extrema and reaches a maximum on going from the multi-domain to the single-domain structure, *i.e.*, at a particle size of about 20 nm.[17]

Thus, if mild oxidation causes an increase in the coercive force, the average size (D_m) of cobalt particle is larger than 20 nm; if $D_m < 20$ nm, oxidation leads to a decrease in the coercive force. This technique enables qualitative assessment of supported Co catalysts and select two main groups, *viz.*, catalysts containing larger ($D_m > 20$ nm) and smaller ($D_m < 20$ nm) metal particles.

If the condition $D_m < 20$ nm is met, the size distribution of cobalt particles can be assessed using a known method.[56] It was employed in evaluating the size of cobalt particles in the catalysts Co/Al_2O_3 and Co – 0.1 mass % Pt/Al_2O_3.[54]

The average sizes of metal particles and the dispersions (S^2) of their size distributions for supported Co catalysts are listed in Table 1. As can be seen, promotion by platinum, the addition of saccharose and the reduction of Co/Al_2O_3 catalysts at higher temperatures lead to an increase in the proportion of superparamagnetic particles and, therefore, to a decrease in the average size of cobalt particles. An increase in the proportion of superparamagnetic cobalt particles was reported when the catalyst Co/SiO_2 was promoted by ruthenium and rhenium.[121]

If the catalyst contains only superparamagnetic cobalt particles, the particle size distribution can be determined from the field dependence using the Langevin relation [see Eqn (8)]. It was shown that the Co/SiO_2 catalyst containing superparamagnetic cobalt particles can be prepared by the ammonium method.[122, 123] A comparison of the results of

Table 1. Parameters of the distribution of cobalt nanoparticles in cobalt-containing catalysts.

Catalyst	T_{bac} /°C	D_m /nm	S^2 /nm
15 mass % Co/Al_2O_3	200	7.5	35
	350	7.8	42
	400	8	43
	500	7.9	40
15 mass % Co – 0.1 mass % Pt/Al_2O_3	200	6.4	23
8 mass % Co – 0.1 mass % Re/Al_2O_3	400	13	45
8 mass % Co – 0.1 mass % $Re(Z)/Al_2O_3$	400	5	19

Note. T_{bac} is the calcination temperature of the catalyst before reduction; Z is saccharose.

magnetic measurements with TEM data revealed that the plot of the rate of the reaction $CO + H_2$ (calculated per specific surface area of metallic cobalt) *vs*. average size of cobalt particles passes through a maximum. Smaller cobalt particles have little effect on the CO conversion and chain propagation.[124] Impregnation of silica gel with cobalt acetate also leads to formation of superparamagnetic particles.[121] The magnetic field dependences of the magnetization for Co/SiO_2 catalysts promoted by ruthenium and rhenium are shown in Fig. 25. The absence of hysteresis in the field dependences indicates that the catalyst contains only superparamagnetic particles. Their average particle size calculated using Eqn (8) is 3 – 6 nm.

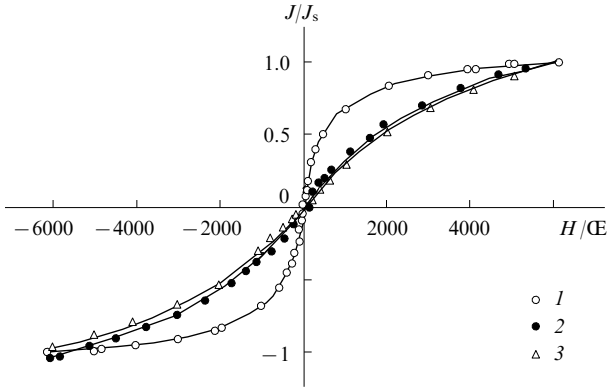


Figure 25. Magnetic field dependences of the magnetization of ruthenium- and rhenium-promoted Co/SiO_2 catalysts.
D /nm: 170 (Co) (*1*), 3.6 (Ru) (*2*) and 3.3 (Re) (*3*).

Superparamagnetic cobalt particles were also obtained by adding saccharose to a Co/SiO_2 catalyst promoted by ruthenium and rhenium.[1,125] Hysteresis in the magnetic field dependence for the Co/SiO_2 catalyst in the absence of saccharose indicates the presence of single-domain and large multi-domain ferromagnetic particles (Fig. 26 *a*). The addition of saccharose to the impregnating solution causes the degree of dispersion of cobalt to increase. Catalysts reduced in pure hydrogen are characterized by the largest proportion of superparamagnetic cobalt particles. According to calculations, the average size of cobalt particles in the Co – Re(saccharose)/SiO_2 catalyst is 4 nm.

The field dependence for the Co – Ru(saccharose)/SiO_2 catalyst is shown in Fig. 26 *b*. The system contains both

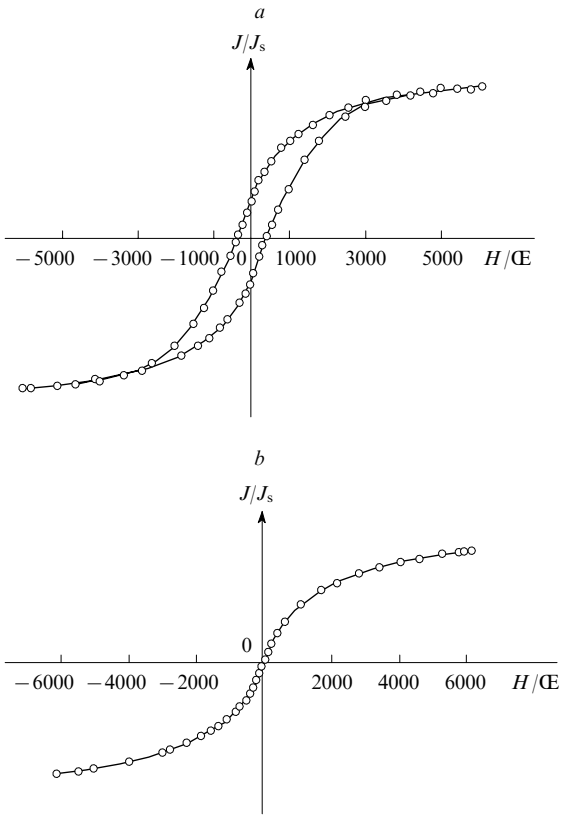


Figure 26. Magnetic field dependences for the catalysts Co – Ru/SiO_2 (*a*) and Co – Ru (saccharose)/SiO_2 (*b*).

single-domain and superparamagnetic cobalt particles. According to calculations using expression (20), the proportion of superparamagnetic particles in the catalyst is about 97% while that of single-domain particles is nearly 3%. Calculations using the Langevin relation [see Eqn (8)] assuming that the contribution of single-domain cobalt particles is negligible (almost no hysteresis loop in the field dependence) gave an average size of cobalt particles in the Co – Re(saccharose)/SiO_2 catalysts of 6 nm.[125]

Superparamagnetic cobalt particles in the Co/Al_2O_3 catalyst can also be obtained by decomposition of cobalt nitrate in glow discharge plasma.[126] The procedure is similar to that used in the case of the Ni/α-Al_2O_3 catalysts.[127] Supports impregnated with cobalt nitrate were dehydrogenated by hexachloroplatinate, dried at 373 K, treated with plasma under mild conditions, decomposed in nitrogen plasma for 45 min at room temperature and then, plasma was reduced in hydrogen for the next 45 min. The catalysts were reduced in H_2 stream at 673 K. It is of great importance that for the Co/Al_2O_3 catalyst in the presence of platinum the dependence of the magnetization on the magnetic field strength shown no hysteresis, *i.e*., all cobalt particles are superparamagnetic.[120] According to calculations using the Langevin relation, the average size of superparamagnetic cobalt particles is nearly 5 nm.

The procedure for preparation is of paramount importance for the final dispersion of cobalt. For the Co/Al_2O_3 catalyst prepared by codeposition and reduced at 773 K, a large proportion of ferromagnetic particles (30 mass %) is blocked at room temperature.[111] The addition of copper by co-impregnation causes the system to exhibit superpara-

magnetism ($D_m \approx 4$ nm). This effect is associated with very high dispersion of cobalt oxide in the presence of precursor.[111] But in the case of conventional impregnation with cobalt and copper such an effect of the copper additive was not observed.[128]

IX. Nickel-containing catalysts

In supported Ni catalysts, only the metal, nickel, exhibits ferromagnetic properties. This is similar to supported Co catalysts. Therefore, interpretation of the magnetic data in this case is somewhat simpler than for supported Fe catalysts. As Co_3O_4 and CoO, nickel oxide is an antiferromagnetic.

Magnetometric studies revealed unique magnetic properties of individual nickel nanoparticles as well as nickel nanoparticles in multiwalled carbon nanotubes (CNTs), which have been widely used recently in catalysis.[129,130] As the size criterion [130] for individual nanoparticles and nickel nanoparticles in multiwalled CNTs, we chose the blockage temperature (T_b), which can be determined from the temperature dependence of the coercive force using Eqn (7).[131,132]

Both systems under study exhibit superparamagnetic properties at temperature $T \geqslant T_b$. In the case of $T \leqslant T_b$, a hysteresis loop is observed in the field dependence of the magnetization. This is characteristic of ferromagnetic single-domain particles and confirms the expected temperature dependence of the parameter H_c.

Only CNTs containing $\leqslant 10\%$ of nickel particles ($D_m = 6-7$ nm) were reported as possessing ferromagnetism.[133,134] It is believed [129] that the reasons are as follows:

— the carbon nanotube precludes the oxidation of nickel;

— the formation and growth of single-domain and one-dimensional system occur at particular anisotropy and outer diameter of the nanotube.

Also, it is believed that there exist two types of interaction, namely, magnetic dipole and exchange interaction.[135] They lead to an increase in external magnetic field which acts on every particle. A remarkable feature is that the coercive force of nickel in CNTs is merely 35 Œ (*cf.* ~80 Œ for bulk nickel).[129] High coercive force of nickel in CNTs can be explained by high effective anisotropy of the system formed by those nickel particles that are constituents of thin carbon cells.[131]

The coercive force of multifunctional nanocomposites with inclusions of catalytically active nickel nanoparticles is relatively high (138.4 Œ) and the ratio of the residual magnetization to the saturation magnetization is 0.325.[136]

X. Comparison of magnetometric methods with other methods of investigation of supported catalysts

Magnetometric methods can be used only if catalysts contain ferromagnetic metals or ferrimagnets such as magnetite. These methods provide the following information on the catalyst structure:

— the number of ferromagnetic phases,

— the average size and size distribution of ferromagnetic particles,

— the mechanisms of formation of various carbides and oxide phases in iron catalysts.

In addition, continuous magnetization measurements offer great prospects for investigation of the kinetics of topochemical reactions involving ferromagnetic metals and their compounds. Changes in the magnetization on chemisorption can give information on the stoichiometry of chemisorption, especially for the nickel catalysts. By measuring the saturation magnetization one can estimate the proportion of the ferromagnetic phase and calculate the degree of reduction in the steady state and at any instant during the pre-treatment and in the course of catalytic reaction. The field dependences allow the size of ferromagnetic particles to be determined. A key feature of the method of continuous magnetization measurements is that information on the structure of a catalyst can often be obtained *in situ*, whereas other methods are of low utility for these purposes.

The advantage of combining the method of continuous magnetization measurements with TPR consists in the possibility to use pure hydrogen instead of diluted hydrogen (5% – 10% H_2 + inert gas) used conventionally. As mentioned above, the thermodynamic parameters of reduction of nanoparticles are size-dependent. This should be taken into account in the TPR studies of catalysts.

The rate and degree of reduction strongly depend on the partial pressure of hydrogen.[98] Thus, the degree of reduction calculated from TPR data is much lower than that determined when the catalyst was reduced in pure hydrogen. Reduction of transition metal oxides often involves a number of steps,[128,137,138] *e.g.*,

$$Co_3O_4 + H_2 \longrightarrow CoO,$$

$$CoO + H_2 \longrightarrow Co.$$

These stages correspond to peaks in the TPR spectra.[73] In the case of Co-supported catalysts, only metallic cobalt exhibits ferromagnetic properties; therefore, the increase in magnetization is associated with the increase in the content of metallic cobalt.

The degree of reduction can also be determined by spectroscopic methods, *e.g.*, X-ray photoelectron spectroscopy (XPS), XRD and EXAFS.[139] However, the accuracy of measurements depends on the quality of spectra, which often represent a number of signals from different reduced and oxidized phases. Experiments are carried out using reduced catalysts in the quasi-stable state, whereas the magnetometric method is applicable to catalysts containing the active component in the transition state. Probably, these difficulties will be overcome with the development of EXAFS and fast EXAFS spectroscopies.[140,141]

Magnetometric methods also give quantitative information on the particle size and particle size distribution. Undoubtedly, if a catalyst contains both single- and multidomain ferromagnetic particles, the particle size can be evaluated only qualitatively. The size of metal particles in supported catalysts can also be determined by XRD, TEM and EXAFS. Taking into account the polycrystallinity of small metal and oxide particles in the supported catalysts, the particle size can be calculated from XRD data using the Scherrer equation or the Williamson – Hall method.[142] The models by Kerkhof – Moulijn [143] and by Kuipers *et al.*[144] are also used to evaluate the size of nanoparticles from XRD data. These models are highly reliable for samples with metal content $\leqslant 10$ mass %. Simultaneous presence of different oxidized and reduced phases complicates interpretation of XRD data. This method is highly sensitive to the

state of surface of the catalyst,[145] and nonuniform distribution of the active component over the catalyst may strongly affect the final results.

The accuracy of evaluation of the particle size less than 6 nm by XRD is much lower due to a large broadening of diffraction peaks. In addition, diffraction peaks from the support may strongly complicate calculations.

TEM and scanning electron microscopy used to evaluate the particle size of catalysts impose specific requirements to samples.[146] Difficulties arise in the studies of samples with high content of metal because possible aggregation may preclude the determination of the size of individual metal particles. The particle size can change under the action of electron beam, especially if the beam interacts with smaller particles.[147] Electron microscopy measurements are usually carried out in ultrahigh vacuum or at very low pressures.[147] In a real situation, the catalyst structure may significantly change in the presence of gas molecules. Relatively low representativeness of the results obtained by TEM should also be taken into account.

EXAFS spectroscopy (see Refs 140 and 147) is useful for particle size calculations on the length scale from less than 1 nm to 2 nm. For larger particles, the accuracy of this method decreases owing to the lack of correlation between the particle size and the coordination number.[148] The chemisorption technique can be used to determine the number of active sites in the catalyst. The amount of adsorbed gas strongly depends on the stoichiometry of the adsorbent, which is difficult to determine in the case of metallic catalysts. The number of active sites in a supported catalyst depends on the degree of reduction of the metal and on the particle size. When using the chemisorption method, it is impossible to separate the contributions of the active sites that depend on the dispersion of the metal and on the degree of reduction.

XI. Conclusion

Magnetometric methods of investigation of supported catalysts combined with conventional spectroscopic methods including HR TEM, absorption spectroscopy, XPS, XRD, TPR, TPO, as well as the temperature-programmed reaction, response and chemisorption methods allow one to obtain additional vast (sometimes, unexpected) information on the systems containing ferro- and ferrimagnetic substances.

Very small ferromagnets are often unstable in air. Therefore, it seems appropriate to study small ferromagnetic species using the *in situ* and *operando* approaches.

Magnetometric methods are the best for investigations of Co- and Ni-containing supported catalysts because only the metal exhibits ferromagnetism; this significantly simplifies interpretation of the magnetic properties. Noteworthy, the Curie temperature of metallic cobalt is much higher than that of iron and nickel. This allows one to study cobalt nanoparticles by magnetic measurements in the stage of pretreatment of most catalysts and in the course of catalytic reactions, such as the Fischer – Tropsch synthesis.

Also, supported catalysts exhibit unique features from the standpoint of a researcher who studies the magnetic properties of nanoparticles. As mentioned above, magnetic dipole – dipole interactions in supported catalysts with large specific surface area are very weak; this significantly facilitates physical measurements in the case of small ferromagnetic particles.

References

1. A Y Khodakov, W Chu, P Fongarland *Chem. Rev.* **107** 1692 (2007)
2. E Iglesia *Appl. Catal., A* **161** 59 (1997)
3. M Dry *Catal. Today* **71** 227 (2002)
4. P A Chernavskii, V V Lunin *Kinet. Katal.* **34** 531 (1993) [a]
5. P A Chernavskii, J-A Dalmon, N S Perov, A Y Khodakov *Oil Gas Sci. Technol.* **64** 25 (2009)
6. P W Selwood *Chemisorption and Magnetisation* (New York: Academic Press, 1975)
7. J T Richardson *J. Appl. Phys.* **49** 1781 (1978)
8. J-A Dalmon, in *Catalysts Characterization, Physical Techniques for Solid Materials* (New York: Plenum, 1994) p. 585
9. P A Chernavskii *Ros. Khim. Zh.* **46** (3) 19 (2002) [b]
10. P E Jacobson, P W Selwood *J. Am. Chem. Soc.* **76** 2641 (1954)
11. P W Selwood *Magnetochemistry* (2nd Ed.) (New York: Interscience, 1956)
12. P Weiss, R Forrer *Ann. Phys.* **5** (1926)
13. S Foner *Rev. Sci. Instrum.* **30** 548 (1959)
14. P A Chernavskii, Doctoral Thesis in Chemical Sciences, Moscow State University, Moscow, 2001
15. V V Kiselev, P A Chernavskii, V V Lunin *Zh. Fiz. Khim.* **61** 280 (1987) [c]
16. P A Chernavskii, A Y Khodakov, G V Pankina, J-S Girardon, E Quinet *Appl. Catal., A* **306** 108 (2006)
17. Yu I Petrov *Fizika Malykh Chastits* (The Physics of Small Particles) (Moscow: Nauka, 1982)
18. J Frenkel, J Dorfman *Nature (London)* **126** 274 (1930)
19. E I Kondorskii *Izv. Akad. Nauk, SSSR, Ser. Fiz.* **16** 398 (1952) [d]
20. E I Kondorskii *Izv. Akad. Nauk, SSSR, Ser. Fiz.* **42** 1638 (1978) [d]
21. J Brown *Micromagnetics* (New York: Wiley, 1963)
22. E. Kneller *Magnetism and Metallurgy* (Eds A E Berkowitz, E Kneller) (New York: Academic Press, 1969) p 365
23. D L Leslie-Pelecky, R D Rieke *Chem. Mater.* **8** 1770 (1996)
24. E C Stoner, E P Wohlfarth *Proc. Phys. Soc.* **240** 599 (1948)
25. C Chen, O Kitakami, Y J Shimada *Appl. Phys.* **84** 2184 (1998)
26. L C R Neel *Acad. Sci.* **228** 664 (1949)
27. L J Weil *Chim. Phys.* **17** 263 (1954)
28. E P Wohlfarth *J. Phys. F* **10** L241 (1980)
29. C P Bean, J D Livingston *J. Appl. Phys.* **30** S120 (1959)
30. J P Chen, C M Sorensen, K J Klabunde, G C Hadjipanayis *Phys. Rev. B* **51** 11527 (1995)
31. I M L Billas, A Chatelain, W A de Herr *Science* **265** 1682 (1994)
32. H Suhl, B H Bertram *J. Appl. Phys.* **82** 6128 (1997)
33. M Primet, J A Dalmon G A Martin *J. Catal.* **46** 25 (1977)
34. G A Martin *Rev. Phys. Appl.* **16** 181 (1981)
35. C Estournés, T Lutz, J Happich, T Quaranta, P Wissler, J L Guille *J. Magn. Magn. Mater.* **173** 83 (1997)
36. J T Richardson, P Desai *J. Catal.* **42** 294 (1976)
37. J A Potton, G J Daniell, A D Eastop *Mon. Not. R. Astron. Soc.* **211** 111 (1984)
38. J Skilling, R K Bryan *J. Magn. Magn. Mater.* **39** 95 (1983)
39. H G Zolla, F Spaepen *Mater. Sci. Eng. A* **204** 71 (1995)
40. A H Baston, J A Potton, M V Twigg, C J Wright *J. Catal.* **71** 426 (1981)
41. L Weil *J. Chim. Phys.* **51** 715 (1954)
42. A Kákay, M W Gutowski, L Takacs, V Franco, L K Varga *J. Phys. A* **37** 6027 (2004)
43. V V Emel'yanov, V V Kureichik, V M Kureichik *Teoriya i Praktika Evolyutsionnogo Modelirovaniya* (Theory and Practice of Evolutionary Modelling) (Moscow: Fizmatlit, 2003)
44. V V Kokorin, A E Perekos, K V Chuistov *Fiz. Magn. Mater.* **43** 966 (1977)
45. E S Venttsel', L A Ovcharov *Teoriya Veroyatnosti* (Theory of Probability) (Moscow: Nauka, 1969)
46. O Kitakami, H Sato, Y Shimada, F Sato, M Anaka *Phys. Rev. B* **56** 13849 (1997)
47. J Sort, S Surinach, J S Muñoz, M D Baró, M Wojcik, E Jedruka, S Nadolski, N Sheludko, J Nogugs *Phys. Rev. B* **68** 014421 (1997)
48. P A Chernavskii *Kinet. Katal.* **46** 1 (2005) [a]

49. N S Perov, A A Bagrets, N Yu Sudarikova, A A Bagrets *J. Magn. (Korean Magn. Soc.)* **8** 1 (2003)
50. N S Perov, A A Radkovskaya, in *Proceedings of 1st and 2nd Dimensional Magnetic Measurement and Testin, Bad Gastein, 2000* p. 104
51. K Yakushiji, S Mitani, K Takanachi, J-G Ha, H Fujimori *J. Magn. Mater.* **212** 75 (2000)
52. J Weissmuller, A Michels, J G Barker, A Wiedenmann, U Erb, R D Shull *Phys. Rev. B.* **63** 214414 (2001)
53. W F Brown Jr *Ann. N.Y. Acad. Sci.* **147** 463 (1969)
54. P A Chernavskii, V Chu, A Yu Khodakov, G V Pankina, N V Peskov *Zh. Fiz. Khim.* **82** 1083 (2008) [c]
55. A S Lermontov, Candidate Thesis in Chemical Sciences, Moscow State University, Moscow, 2002
56. J A Dalmon, G A Martin, B Imelik *Surf. Sci.* **41** 587 (1974)
57. J M Zowtiak, C H Bartholomew *J. Catal.* **83** 107 (1983)
58. C R Abeledo, P W Selwood *J. Chem. Phys.* **37** 2709 (1962)
59. J A Dalmon, G A Martin, B Imelik *Jpn. J. Appl. Phys. Suppl.* **2** (2) 261 (1974)
60. J Deportes, J P Rebouillat, R Dutartre, J A Dalmon, G A Martin *C.R. Seances Acad. Sci., Ser. C* **276** 1393 (1973)
61. J A Dumesic, H Topsøe, M Boudart *J. Catal.* **37** 513 (1975)
62. R Detartre, P Bussiere, J-A Dalmon, G A Martin *J. Catal.* **59** 383 (1979)
63. J A Dalmon, M Primet, G A Martin, B Imelik *Surf. Sci.* **50** 95 (1975)
64. T Hill, M Mozaffari-Afshar, J Schmidt, T Risse, S Stempel, M Heemeier, H-J Freund *Chem. Phys. Lett.* **292** 524 (1998)
65. Yu I Petrov *Klastery i Malye Chastitsy* (Clusters and Small Particles) (Moscow: Nauka, 1986)
66. G B Sergeev *Ros. Khim. Zh.* **46** 22 (2002) [b]
67. T L Hill *Thermodynamics of Small Systems* (New York: Benjamin Inc., 1963)
68. I D Morokhov, V I Petinov, L I Trusov, V F Petrunin *Usp. Fiz. Nauk* **133** 653 (1981) [e]
69. A I Gusev *Nanomaterialy, Nanostruktury, Nanotekhnologii* (Nanomaterials, Nanostructures and Nanotechnologies) (Moscow: Fizmatlit, 2005)
70. O M Poltorak *Lektsii po Khimicheskoi Termodinamike* (Lectures on Chemical Thermodynamics) (Moscow: Vysshaya Shkola, 1971)
71. P A Chernavskii *Zh. Fiz. Khim.* **78** 1416 (2004) [c]
72. H Bi, W Cai, C Kan, L Zhang, D Martin, F Träger *J. Appl. Phys.* **92** 7491 (2002)
73. G S Sewell, E van Steen, C T O'Connor *Catal. Lett.* **37** 255 (1996)
74. P A Chernavskii, A S Lermontov, G V Pankina, S N Torbin, V V Lunin *Kinet. Katal.* **43** 292 (2002) [a]
75. P A Chernavskii, V V Kiselev, L I Baranova, A P Kuprin, A N Grechenko, V V Lunin *Zh. Fiz. Khim.* **65** 1675 (1991) [c]
76. P A Chernavskii, V V Kiselev, V V Lunin *Zh. Fiz. Khim.* **66** 2712 (1992) [c]
77. P A Chernavskii, G V Pankina, I N Zavalishin, V V Lunin *Kinet. Katal.* **35** 126 (1994) [a]
78. P A Chernavskii, G V Pankina, V V Lunin *Zh. Fiz. Khim.* **72** 3089 (1998) [c]
79. P A Chernavskii, G V Pankina, A N Grechenko, V V Lunin *Zh. Fiz. Khim.* **67** 18 (1993) [c]
80. V V Kiselev, G V Pankina, P A Chernavskii, V V Lunin *Zh. Fiz. Khim.* **65** 839 (1991) [c]
81. P A Chernavskii, V V Lunin *Kinet. Katal.* **34** 531 (1993) [a]
82. V R Elías, M I Oliva, S E Urreta, S P Silvetti, K Sapag, A M M Navarro, S G Casuscelli, G A Eimer *Appl. Catal., A* **381** 92 (2010)
83. L A Cano, M V Cagnoli, N A Fellenz, J F Bengoa, N G Gallegos, A M Alvarez, S G Marchetti *Appl. Catal., A* **379** 105 (2010)
84. D Bianchi, L-M Tau, S Borkar, C O Bennett *J. Catal.* **84** 358 (1983)
85. A F H Wielers, A J H M Kock, C E C A Hop, J W Geus, A M van der Kraan *J. Catal.* **117** 1 (1989)
86. C J Wang, J G Ekerdt *J. Catal.* **80** 172 (1983)
87. J A Amelse, J B Butt, L H Schwartz *J. Phys. Chem.* **82** 558 (1978)
88. A Ya Rozovskii *Geterogennye Khimicheskie Reaktsii. Kinetika i Makrokinetika* (Heterogeneous Chemical Reactions. Kinetics and Macrokinetics) (Moscow: Nauka, 1989)
89. C H Bartolomew *Hydrogen Effect in Catalysis. Fundamental and Practical Applications* (Basel, New York: Marcel Dekker, 1988)
90. Yu B Kryukov, Doctoral Thesis in Chemical Sciences, Institute of Petrochemical Synthesis, Academy of Sciences of the USSR, Moscow, 1969
91. G P Van der Laan, A A C M Beenackers *Catal. Rev. Sci. Eng.* **41** 255 (1999)
92. J W Niemantsverdriet, A M van der Kraan, W L van Dijk, H S van der Baan *J. Phys. Chem.* **84** 3363 (1980)
93. J B Butt *Catal. Lett.* **7** 61 (1990)
94. A J H Kock, H M Fortuin, J W Geus *J. Catal.* **96** 261 (1985)
95. H Matsumoto, C O Bennett *J. Catal.* **53** 331 (1978)
96. S M Loktev, L I Makarenkova, E V Slivinskii, S D Entin *Kinet. Katal.* **13** 1042 (1972) [a]
97. E E Unmuth, L H Schwartz, J B Butt *J. Catal.* **63** 404 (1980)
98. P A Chernavskii, V V Lunin *Kinet. Katal.* **37** 850 (1996) [a]
99. P A Chernavskii *Catal. Lett.* **45** 215 (1997)
100. P A Chernavskii, G V Pankina, V V Lunin *Zh. Fiz. Khim.* **71** 1007 (1997) [c]
101. Y Ichiyanagi, S Yamada *Polyhedron* **24** 2813 (2005)
102. F J Romero, J Jimenez, J Del Cerro *J. Magn. Magn. Mater.* **280** 257 (2004)
103. L Bedel, A C Roger, C Estournes, A Kiennemann *Catal. Today* **85** 207 (2003)
104. L Bedel, A C Roger, J-L Rehspringer, Y van Zimmermann, A Kiennemann *J. Catal.* **235** 279 (2005)
105. Yu D Tretyakov *Termodinamika Ferritov* (Thermodynamics of Ferrites) (Leningrad: Khimiya, 1967)
106. G Rog, B Langanke, G Borchardt, H Schmalzried *J. Chem. Thermodyn.* **6** 1113 (1974)
107. J B Holt *Materials Science Research* (New York: Plenum, 1969)
108. E van Steen, G S Sewell, R A Makhothe, C Micklethwaite, H Manstein, M de Longe, C T O'Connor *J. Catal.* **162** 220 (1996)
109. W Chu, P A Chernavskii, L Gengembre, G V Pankina, P A Forgarland, A Y Khodakov *J. Catal.* **252** 215 (2007)
110. J-S Girardon, A S Lermontov, L Gengembre, P A Chernavskii, A Griboval-Constant, A Y Khodakov *J. Catal.* **230** 339 (2005)
111. J-S Girardon, A Griboval-Constant, L Gengembre, P A Chernavskii, A Y Khodakov *Catal. Today* **106** 161 (2005)
112. H E Kissinger *Anal. Chem.* **29** 1702 (1957)
113. P Grandvallet, Ph Courty, E Freund, in *Proceedings of the 8th International Congress on Catalysis* Vol. 2 (Berlin: Springer, 1984) p. 81
114. Ph Courty, P Chaumette, C Raimbault *Travers Phes. Rev. IFP* **45** 561 (1990)
115. J-A Dalmon, P Chaumette, C Mirodatos *Catal. Today* **15** 101 (1992)
116. J van de Loosdrecht, B Balzhinimaev, J-A Dalmon, J W Niemantsverdriet, S V Tsybulya, A M Saib, P J van Berge, J L Visagie *Catal. Today* **123** 293 (2007)
117. M Bremaud, P Fongarland, J Anfray, S Jallais, D Schweich, A Y Khodakov *Catal. Today* **106** 137 (2005)
118. E van Steen, M Claeys, M E Dry, J van de Loosdrecht, E L Viljoen, J L Visagie *J. Phys. Chem. B* **109** 3575 (2005)
119. K Hauffe *Reaktionen in und an Festen Stoffen* (Berlin: Springer, 1955)
120. N Cabrera, N F Mott *Rep. Prog. Phys.* **12** 163 (1949)
121. G V Pankina, P A Chernavskii, A Yu Khodakov, Zh -S Zhirardon, V V Lunin *Zh. Fiz. Khim.* **80** 845 (2006) [c]
122. A Barbier, A Tuel, I Arcon, A Kodre, G A Martin *J. Catal.* **200** 106 (2001)
123. A Barbier, A Hanif, J-A Dalmon, G A Martin *Appl. Catal., A* **168** 333 (1998)
124. G A Martin, J-A Dalmon, C Mirodatos, in *Proceedings of the 8th International Congress on Catalysis* Vol. 4 (Berlin: Springer, 1984) p. 371

125. J-S Girardon, E Quinet, A Griboval-Constant, P A Chernavskii, L Gengembre, A Y Khodakov *J. Catal.* **248** 143 (2007)
126. W Chu, L-N Wang, P A Chernavskii, A Y Khodakov *Angew. Chem. Int., Ed.* **47** 5052 (2008)
127. Y Zhang, W Chu, W Cao, C Luo, X Wen, K Zhou *Plasma Chem. Plasma Proc.* **20** 137 (2000)
128. J E Baker, R Burch, S J Hibble, P K Loader *Appl. Catal.* **65** 281 (1990)
129. E N Konyushenko, N E Kazantseva, J Stejskal, M Trchova, J Kovářova, I Sapuina, M M Tomishko, O V Demicheva, J Prokeš *J. Magn. Magn. Mater.* **320** 231 (2008)
130. D Gozzi, A Latini, G Capannelli, F Canepa, M Napoletano, M R Cimberle, M Tropeano *J. Alloys Compd.* **419** 32 (2006)
131. B D Cullity, in *Introduction to Magnetic Materials. Series in Metallurgy and Materials* (Reading, MA: Addison-Wesley, 1972)
132. B H Sohn, R E Choen, G C Papaefthymiou *J. Magn. Magn. Mater.* **182** 216 (1998)
133. A A Bukhraev, D V Ovchinnikov, N I Nurgazizov, E F Kukovitskii, M Klaiber, R Wiesendanger *J. Phys. Solid State* **40** 1163 (1998)
134. S V Vonsovskii *Magnetizm* (Magnetism) (Moscow: Nauka, 1971)
135. R S Inshakov, S V Komagortsev, A D Okotrub *Pis'ma Zh. Eksp. Teor. Fiz.* **78** 236 (2003) [f]
136. C He, N Zhao, C Shi, J Li, H Li *Mat. Res. Bull.* **43** 2260 (2008)
137. A Y Khodakov, A Griboval-Constant, R Bechara, F Villain *J. Phys. Chem. B* **105** 9805 (2001)
138. A Y Khodakov, J Lynch, D Basin, B Rebours, N Zanier, B Moisson, P Chaumette *J. Catal.* **168** 16 (1997)
139. C Pichon, J Lynch *Oil Gas Sci. Technol.* **60** 735 (2005)
140. M A Newton, A J Dent, S G Fiddy, B Jyoti, J Evans *Catal. Today* **126** 64 (2007)
141. R Frahm *Nucl. Instrum. Methods Phys. Res., A* **270** 578 (1988)
142. G K Williamson, W H Hall *Acta Metallurg.* **1** 22 (1953)
143. F P J M Kerkhof, J A Moulijn *J. Phys. Chem.* **83** 1612 (1979)
144. H P C E Kuipers, H C E Van Leuven, W M Visser *Surf. Interface Anal.* **8** 235 (1986)
145. G A Somorjai *Introduction to Surface Chemistry and Catalysts* (New York: Willey, 1994)
146. J Lynch *Oil Gas Sci. Technol.* **57** 281 (2002)
147. M Pan, J M Cowley, I Y Chan *Catal. Lett.* **5** 1 (1990)
148. R E Benfield *J. Chem. Soc., Faraday Trans.* **88** 1107 (1992)

[a] — *Kinet. Catal. (Engl. Transl.)*
[b] — *Mendeleev Chem. J. (Engl. Transl.)*
[c] — *Russ. J. Phys. Chem., Ser. A (Engl. Transl.)*
[d] — *Bull. Russ. Acad. Sci., Phys. (Engl. Transl.)*
[e] — *Physics-Uspekhi (Engl. Transl.)*
[f] — *J. Exp. Theor. Phys. Lett. (Engl. Transl.)*